Confined Growth of a Vapour Bubble in a Capillary Tube at Initially Uniform Superheat: Experiments and Modelling

D. B. R. Kenning[1,2], D. S. Wen[3,2], K. S. Das[4,5] and S. K. Wilson[5]

[1]Brunel University, School of Engineering and Design, Uxbridge UB8 3PH, UK

[2]University of Oxford, Department of Engineering Science, Oxford OX1 3PJ, UK

[3]Queen Mary, University of London, Department of Engineering, London E1 4NS, UK

[4]University of Toronto, Department of Physics, Toronto M5S1A7, Canada

[5]University of Strathclyde, Department of Mathematics, Glasgow G1 1XH, UK

E-mail: david.kenning@eng.ox.ac.uk

1st July 2005, revised 22nd December 2005 and 14th February 2006

Abstract

Bubble growth was triggered in a capillary tube closed at one end and vented to the atmosphere at the other and initially filled with uniformly superheated water. Measurements of the rate of axial growth and the varying pressure at the closed end were used to test under these simplified conditions assumptions employed in one-dimensional models for bubble growth applicable to the more complex conditions of confined-bubble flow boiling in microchannels. Issues included the thickness of the liquid films round confined bubbles and changes in saturation temperature due to the changes in pressure generated by bubble motion. Modelling features requiring further attention were identified, such as the possibility of "roll-up" of the liquid film due to a large dynamic contact angle.

Keywords: Confined bubble growth, boiling in microchannels

1 Introduction

Miniaturization of engineering systems such as micro-electronic circuits, chemical micro-reactors and fuel cells leads to ever-increasing requirements for the removal of heat fluxes exceeding 1 MW/m^2 from areas of a few square centimeters. One way of meeting these requirements is to employ flow boiling heat transfer in microchannels fabricated into the system carrier, e.g. a silicon chip [1]. For reasons of manufacture, the channels are likely to be of non-circular cross-section and thermo-fluid considerations define the potential range of dimensions as 50–1000 μm. At this scale, surface tension forces influence the lateral and axial distribution of liquid and vapour so that the physics of boiling are considerably modified compared to boiling in channels with much larger cross-sections. Empirical correlations and regime-based models for heat transfer and pressure drop developed for large channels are not reliable guides for micro- and mini- channels and heat transfer performance is limited by transient downstream dryout, e.g. [2]. It is essential to develop predictive methods with a sound physical basis. This reduction in scale presents both a challenge and an opportunity, because flow and heat transfer are influenced by the dynamics of a small group of bubbles, rather than the averaged behaviour of a large population of bubbles, improving the prospects of developing mechanistic models. Such development is facilitated by localized experimental observations of bubbles with synchronized measurements of the resulting fluctuations in local conditions such as temperature, pressure and wall heat flux.

Yan and Kenning [3, 4] observed flow patterns synchronised with measurements of local fluctuations in pressure and wall temperature at five positions along a single, thin-walled mini-channel of rectangular cross-section 2 mm $\times$ 1 mm for water in the confined-bubble flow regime at atmospheric exit pressure. They traced the axial propagation of pressure pulses accompanying the acceleration of liquid slugs by the growth of confined bubbles, confirming the mechanism proposed and modelled by Kew and Cornwell [5]. The associated changes in local saturation temperature were of similar magnitude to the time-averaged wall superheat, indicating a significant effect on heat transfer that was noted but not modelled in [5]. At a given position, there was a cycle in time through three heat transfer regimes: single-phase convection to the liquid slug, evaporation of a smooth film round the confined bubble and nucleate boiling in the film. The heat transfer coefficients for the three regimes only varied by $\pm$ 20% in this

particular case and, perhaps for this reason, the large effect of high or low compressibility of the upstream supply on temporary flow reversals and the power distribution functions of the pressure and temperature fluctuations had little effect on the time-averaged heat transfer coefficient. This may not always be true, and observations are required over a much wider range of conditions. Brutin and Tadrist [6, 7] observed similar behaviour for n-pentane boiling in a single 4 mm $\times$ 1 mm channel, in which controlled upstream compressibility influenced heat transfer. Flow reversals reduce the critical heat flux [8] and upstream compressibility is present in assemblies of parallel microchannels, whatever the nature of the pump supplying liquid, unless corrective measures are applied to each channel [9]. Wen et al. [10] extended the analysis of the data in [3, 4] to a lower mass flux of 57 kg/m^2 s and found indirect evidence of transient dryout initiating upstream and propagating downstream with bubbles, even at very low heat fluxes, which did not occur at higher mass fluxes. This sort of dryout is likely to be sensitive to the wetting characteristics of the fluid/wall combination and lateral retraction of the liquid film towards the corners by the combination of surface tension forces and evaporation.

Zhang et al., in studies summarized in [11, 12], measured pressure and temperature fluctuations of greatly increased magnitude for water boiling in channels of much smaller rectangular cross-section with dimensions in the range 50–170 μm. The amplitude of the pressure fluctuations could reach 140 kPa, sufficient for a risk of mechanical damage, as well as causing large transient changes exceeding 6 K in the saturation temperature. They found that reduction in size below 80 μm led to a change in flow regime from confined-bubble flow to a fluctuating, sudden transition from liquid-only flow to mist flow with reduced heat transfer coefficients, unless artificial nucleation sites were provided. In order to obtain high heat transfer coefficients, they recommended operation in what they termed annular flow at low exit qualities in the range 0.1–0.3. Under these conditions, it is likely that the annular films are formed round long confined bubbles separated by liquid slugs. Modelling of heat transfer in the confined-bubble flow regime at a level that includes the effect of pressure fluctuations is therefore of high priority.

Models for confined-bubble flow boiling may be implemented at different levels of realism, but always involve some approximations to the physics, such as the assumption that transport processes in the vapour are sufficiently rapid to maintain the equilibrium relationship between vapour pressure and saturation temperature at the bubble interfaces. In principle

two-dimensional and three-dimensional computational fluid dynamics (CFD) numerical simulations minimise the approximations about the behaviour of the liquid phrase, but they involve practical difficulties in accurately representing the moving, deformable interfaces and the transport of heat and mass across them, particularly at moving contact lines. Nevertheless they provide valuable insights into situations with complex geometry, such as that studied by Mukherjee and Kandlikar [13, 14] who investigated asymmetrical growth of a vapour bubble near the entrance to a channel of rectangular cross-section from nucleation on one wall through to the early stages of confined growth and the development of dryout on the walls. Although not done in these particular examples, the simulations are capable of modelling the variations in interfacial temperature caused by the pressure variations in the liquid and vapour. The penalties for simulation at this level of detail are an increased ratio of computing to real time and/or limitations on the size of the computational domain. Some studies may require simulations of the entire length of the channel over long run times, e.g. for the investigation of heat transfer stability during changes in heat load, stochastic modulation of the nucleation frequency or disturbances from neighbouring channels. Then it may be more practicable to use one-dimensional flow models incorporating correlations or analytical sub-models for features such as film thickness, heat transfer coefficients and wall shear stress.

A state-of-the-art example of a one-dimensional model by Thome et al. [15, 16] considers cyclic variations due to the passage of groups of three heat transfer regions that change in length as they progress downstream, namely a liquid slug and a confined bubble with a liquid film that evaporates to a dry patch at the rear of the bubble. Steady-state correlations for axially developing single-phase heat transfer coefficients are used for the liquid-only and vapour-only regions. Evaporation of the liquid film from an initial thickness δ_0 to a defined minimum thickness $\delta_{\min}$ is driven by the uniform wall heat flux, transferred across the film by conduction, implying a fully-developed linear temperature profile across the film at all positions. (Nucleate boiling in the thin film is not considered.) The initial film thickness is obtained from a modification of a correlation developed by Moriyama and Inoue [17] from experiments on radial growth of cylindrical bubbles triggered in uniformly superheated R113 between parallel plates (discussed in more detail in Section 6) including a correction factor C_{δ_0}. The group formation frequency f depends on a model for bubble nucleation and growth to confinement, involving a further correction factor. The values of the three disposable quantities, $\delta_{\min}$, C_{δ_0} and f, were

determined by achieving the best fit of the time-averaged heat transfer coefficients to nine sets of data for refrigerants and one for carbon-dioxide. Their values varied quite widely between sets [16]. This model does not calculate the pressure fluctuations caused by the dynamics of the liquid slugs and the consequent fluctuations in the saturation temperature, which is the reference temperature for the fluctuating heat transfer coefficient. Some other models of this sort, e.g. for pulsating heat pipes [18, 19], do include schemes for calculating the pressure variations in trains of liquid slugs and expanding confined bubbles, but do not model the thin films and assume a constant heat transfer coefficient in the thin-film region. Models for pressure fluctuations should be added to one-dimensional models such as [15] for confined-bubble flow boiling. Further development of the correlations in the models should reduce the requirement for empirical determination of the values of coefficients for particular fluids.

The present work was undertaken to obtain experimental data for confined bubble growth under simpler conditions than occur in flow boiling that can be used to test modelling assumptions concerning the thickness of the liquid film round a long bubble and the transfer of heat across it, and the pressure difference across the liquid column ahead of the bubble due to viscous resistance and inertial loading under highly transient conditions with large accelerations. The experiments were designed to eliminate any influence of entry flow conditions and disturbances from preceding bubbles by triggering growth of a single bubble in a transparent capillary tube, closed at one end and initially containing uniformly superheated water. Even with this simplification, it proved more difficult than was expected to achieve boundary and initial conditions that could be specified precisely in a one-dimensional model, as will be discussed later.

The experiment is a variant on that of Moriyama and Inoue [17] on radial growth of cylindrical bubbles between parallel plates, in which the pressure rise in the bubbles was not considered and may have been small. The capillary tube geometry accentuates the pressure difference required to overcome the viscous and inertial resistance of the liquid expelled by the bubble. It is difficult to install inside a capillary tube the sensors required for local, transient measurement of the film thickness and wall shear stress. Film thickness is often inferred from transient heat transfer measurement and a heat transfer model, rather than direct measurement. Moriyama and Inoue calculated wall heat fluxes from measurements of transient temperatures on their flat walls at several radial distances from the point at which the bubble growth was triggered.

They assumed that the sudden cessation in cooling corresponded to dryout of the film by evaporation and calculated the original thickness from a heat balance. In [3, 4] film thicknesses were estimated from instantaneous heat transfer coefficients by assuming steady conduction throughout the film. Transient temperature measurements were not attempted in the present study. Only the initial uniform temperature, the varying pressure at the closed end of the tube, and the varying length of the bubble were measured. As in the model of Thome et al. [15] for the more complicated situation of flow boiling, the model linking the observed quantities depends on the interaction of several parameters, for which values must be deduced by fitting the model to the experimental observations. It will be shown that the measurement of pressure makes it possible to examine some aspects of the model for the motion of the liquid column separately from the combined thermal and fluid-dynamical model for the bubble growth. So far, the technique has been demonstrated only for a limited range of conditions for water in a glass capillary tube of circular cross-section. In principle the technique is applicable to a wider range of conditions, including mixtures in channels of non-circular cross-section.

2 Experiment

Growth of a single bubble in initially stationary, uniformly superheated water in a vertical, borosilicate glass capillary tube was triggered by transient electrical heating of a small resistance wire near the lower, closed end of the tube. The upper end of the tube was vented to the atmosphere. The varying gauge pressure at the closed end was measured by a miniature pressure transducer and the length of the bubble was recorded by a high-speed video camera.

The apparatus is shown schematically in Fig.(1). Experiments were performed with borosilicate glass tubes of internal diameters 0.8 $\pm$ 0.04 mm and 0.48 $\pm$ 0.024 mm, with the same external diameter of 1.8 mm and length 150 mm. A 0.1 mm hole was bored 15 mm from the lower end of each tube to accommodate a 50 μm diameter nichrome triggering wire, U-shaped to accommodate thermal expansion and sealed in place with epoxy cement. Connections to the computer-controlled, pulsed power supply were soldered to the wire outside the tube and held by more epoxy cement. This end of the tube was cemented into the plastic housing of a miniature pressure transducer, into which a second hole was bored for connection through micro-valve 1 to a filling syringe. The other end of the tube was cemented to a "Tee" connector to a solenoid exhaust valve and, through micro-valve 2 on the side-arm, a nitrogen gas

supply at a pressure controlled by a precision regulator. The fragile capillary tube was held by thermally-conducting cement in a groove machined in a copper support plate equipped with three calibrated thermocouples and a serpentine electrical heating element connected to a variable transformer. The assembly was mounted in a transparent, thermally-insulating box.

In order to avoid uncontrolled bubble nucleation, the tube was cleaned by soaking with dilute detergent solution overnight, followed by prolonged flushing with water that had been degassed by boiling in a separate vessel. The tube was then emptied and heated to its operating temperature for calibration of the pressure transducer by nitrogen supplied through valve 2 at a gauge pressure measured by a precision transducer with an accuracy of $\pm$ 0.1 kPa. Atmospheric pressure P_A was taken as the daily average value recorded by the local meteorological station, without allowance for diurnal variations. The tube was then filled with subcooled degassed water through valve 1, with valve 2 closed and the exhaust valve open, until the water level was just visible below the upper connector. Valve 1 was then closed and the system was slowly reheated to the desired superheat relative to atmospheric pressure. Bubble growth was triggered when the three thermocouples on the copper plate recorded the same initial temperature T_0 to within 0.2 K. The maximum uncertainty in the initial superheat due to the uncertainties in initial temperature and atmospheric pressure was estimated to be 0.4 K. At superheats below 3 K, the superheating could be performed with the exhaust valve open without nucleation occurring prior to the triggering pulse. At higher superheats, it was necessary to deactivate stray nucleation sites by prepressurization of the liquid [20], i.e. by applying a high gas pressure through valve 2 with the exhaust valve closed. The strength of the seal round the trigger wire limited this pressure to 53 kPa gauge pressure, although a higher pressure would have been desirable. Valve 2 was then closed, ready for superheating by opening the exhaust valve. Pressure traces for the two procedures are shown in Fig.(2). In each case, growth was triggered when the recorded pressure was atmospheric pressure plus the hydrostatic pressure of the liquid column. There was a delay of 10–15 ms before there was a detectable increase in pressure, corresponding approximately to the time required for a spherical bubble to grow from microscopic size to fill the cross-section of the tube. Bubble growth was recorded by a video camera at 200 or 500 Hz, synchronized with the pressure signal by a pulse to a LED at a set interval before the triggering pulse. The cement sealing the trigger wire obscured the bubble until it had grown to a length of approximately 5 mm,

so the earliest stages of growth to a confined state could not be observed. The requirement to track the front of the bubble over a distance of up to 120 mm placed a constraint on the camera spatial resolution of 0.2 mm per output pixel so the uncertainty in the position of the front of the bubble, obtained by reference to a scale with 1 mm graduations mounted alongside the tube, was conservatively estimated to be ± 0.5 mm at velocities up to 4 m/s. The bubble front was less distinct at higher velocities attained at the highest superheat. In most of the tests, the field of view of the camera was restricted to the first 80 mm of the tube in order to improve the resolution. The precautions against uncontrolled nucleation did not always work but multiple bubbles were detected from the video recording and the data discarded.

3 Experimental Data

Only five complete sets of data were obtained in the series of tests reported here because of the difficulties of constructing the apparatus and performing the experiments, so it was not possible to investigate reproducibility. All the tests were for water with bubble growth initiated and terminating at atmospheric pressure and with an initial liquid column length of nominally 120 mm. Four tests were performed without initial prepressurization, at superheats of 1.6 K, 2.2 K in 0.48 mm diameter tubes and 1.5 K, 2.2 K in 0.80 mm diameter tubes. The one test that required prepressurization to suppress unwanted nucleation was at a superheat of 3.7 K in a 0.48 mm tube. Test runs are here designated by the tube diameter/superheat, e.g. 0.48/3.7.

The basic data for upstream gauge pressure $P(t) - P_A$ and bubble length $Z(t)$ are shown in Fig.(3), together with plots of the bubble nose velocity $U_B(t)$, derived by differentiation of the raw data for $Z(t)$. Time $t = 0$ corresponds to the triggering pulse. There was no record of a pressure disturbance at the instant of triggering. After an initial delay, the bubble length increased rapidly. The pressure increased to a maximum and then declined. The very small residual pressures at the end of some runs may have been due to retention of liquid in the exhaust valve. The time of the maximum pressure is indicated by a dotted line linking each set of graphs. The plots of bubble velocity U_B have small plateaux at, or slightly after, the maximum pressure and there are some indications of oscillatory behaviour that may be genuine or may be due to the effect of experimental errors on the differential of $Z(t)$. Run 0.48/3.7 had the highest growth rate, with the strongest indications of fluctuations in the velocity near the peak pressure. The liquid velocity U_L is slightly smaller than U_B, because of the liquid film

deposited on the wall, but a bubble Reynolds number of 1000 (with radius as characteristic length), marked on the graphs, is an approximate indicator of the conventional engineering criterion for transition from laminar to turbulent flow at a liquid Reynolds number (based on diameter) of 2000. This does not bear any particular relationship to the occurrence of the maximum pressure, nor is there clear evidence of a change in the character of $U_B(t)$ at this Reynolds number.

The maximum pressures are proportional to the initial superheat relative to atmospheric pressure and inversely proportional to the tube diameter, Fig.(4). This simple relationship may be fortuitous. Nondimensional plots in Fig.(5) of pressure difference against bubble length, normalised respectively with the pressure difference corresponding to the vapour pressure at the initial temperature $P_S(T_0) - P_A$ and the length of the tube L, reveal that the pressure variations during the runs were less similar than they appear in Fig.(3). In the 0.48 mm tube, the maximum pressure was, within experimental uncertainty, close to the limit on vapour pressure set by the initial superheat; in the 0.80 mm tube it was significantly lower. The bubble length at which the maximum pressure was reached increased with increasing superheat. The length of the bubble as it approached the end of the tube was not recorded in four of the runs because of limitations on the field of view of the camera. The plot in Fig.(5) for run 0.48/3.7 at the highest superheat (and the only run with prepressurization) cut across the other runs and had a pronounced concave shape in its later stages.

4 Basic Models for Bubble Growth

4.1 Growth from Nucleation to Confinement

The initial conditions for the confined-growth model depend on the preceding growth from triggered nucleation on a heated wire to a radius approximately equal to the tube radius R in time t_0, Fig.(6a). This growth is estimated by the well-established model for spherical, unconfined bubble growth at constant superheat and pressure, e.g. [21]:

$$t_0 = \frac{R^2}{\alpha_L Ja^2 {C_B}^2}, \tag{1}$$

where Ja is the Jakob number

$$Ja = \frac{\rho_L c_L (T_0 - T_{S0})}{\rho_V h_{LV}}, \tag{2}$$

and the unconfined bubble growth factor C_B is a constant that is expected to have a value in the range $\sqrt{4/\pi}$–$\sqrt{12/\pi}$. The heat flux to the bubble interface is then

$$q_H = \frac{C_B k_L (T_0 - T_{S0})}{2\sqrt{\alpha_L t_0}}. \tag{3}$$

This model does not take into account the gradual transition from unconfined to confined growth simulated for more complicated conditions in [13, 14] and described by an approximate model by Yuan et al. [22]. The assumption of constant pressure during growth immediately following nucleation is consistent with the experimental measurements of $P(t)$.

4.2 Confined Growth

The confined bubble is modelled as having hemispherical ends joined by a cylinder of length $Z(t)$ surrounded by a liquid film of initial thickness $\delta(Z)$, Fig.(6b). The interface of the bubble and the mass of vapour $M(t)$ within it are assumed to be at a temperature that adjusts instantly to the saturation temperature $T_S(P)$ corresponding to the uniform vapour pressure $P(t)$ within the bubble. For the particular conditions of these experiments with no incoming flow of liquid, the rear of the bubble near the pressure transducer is assumed to remain stationary. Vapour evaporated from the liquid film reaches a maximum mean velocity equal to that of the bubble nose, U_B, and the estimated pressure differences along the length of the bubble are negligible compared to the pressure difference required to propel the liquid column. The changes in P with time are small enough for $T_S(P)$ relative to reference conditions at atmospheric pressure to be calculated from the linearized Clausius-Clapeyron equation

$$T_S - T_{SA} = \frac{T_{SA}}{\rho_{VA} h_{LV}} (P - P_A), \tag{4}$$

with the corresponding saturated vapour density given by

$$\rho_V - \rho_{VA} = \frac{\rho_{VA}}{P_A} \left[1 - \frac{T_{SA} P_A}{\rho_{VA} h_{LV}} \right] (P - P_A). \tag{5}$$

The model requires simultaneous numerical solution of the equation of state of the vapour, the energy balance at the interface, the continuity equation relating the bubble and liquid velocities and the momentum equation for the liquid, together with prescriptions for the film thickness δ, the heat fluxes through the cylindrical and hemispherical surfaces and the shear stress τ acting on the liquid column. Simple approximate prescriptions are first used for the solutions described in Section 5. Improved prescriptions are discussed in Sections 6 and 7. The equations are nonlinear and are solved by standard numerical methods.

4.3 Simple Approximations

4.3.1 Film Thickness and Heat Transfer

For initial calculations, it is assumed that the film is created with a specified thickness δ that is the same at all positions along the tube, irrespective of the local velocity and acceleration of the bubble. The development length of a few tube radii required for the film to come to rest relative to the wall behind the nose of the bubble is neglected. The value of δ is chosen to give the best match of the solutions of the equations to the experimental data. It is further assumed that changes in δ due to evaporation are negligible, so that the film does not dry out. New surface is continuously created at the front of the bubble and the heat transfer to this surface is assumed to occur by transient conduction, thus resembling models for unconfined bubble growth, except that the surface temperature changes as the pressure changes with time and the diffusion of heat eventually penetrates into the adjacent solid wall. The heat flux to an element of the film is initially infinite and decreases with the age of the element.

It will be noted that this model for heat transfer differs considerably from that used in the Thome et al. [15] model summarized in Section 1, which assumes that the film and the wall are sufficiently thin for a constant heat flux through the film to be established immediately, and that the combination of initial film thickness, liquid properties (particularly the latent heat of evaporation) and film lifetime result in large changes in film thickness by evaporation. Which model is more appropriate can only be determined after the film thickness is known. For the particular conditions of the experiments with water in glass tubes described in this paper, film thicknesses are later deduced that are consistent with the use of the transient conduction model and the neglect of change of thickness due to evaporation. Every bubble grows to a volume $\pi R^2 L$, requiring for conservation of mass the evaporation of a volume of liquid $\pi R^2 L \rho_V / \rho_L$, equivalent to a change in thickness Δ of an annular film averaged over the length of the tube given by

$$\Delta = \frac{R\rho_V}{2\rho_L}. \tag{6}$$

For water at atmospheric pressure in tubes of radius 0.24 mm and 0.40 mm, the respective values of Δ are 0.07×10^{-6} m and 0.12×10^{-6} m, compared to estimated film thicknesses in excess of 10^{-5} m.

For these conditions, three further approximations can be made that make it possible to

specify the heat flux to the bubble by an analytical expression, namely

(i) planar geometry is used, instead of cylindrical;

(ii) the liquid film and the tube wall are assumed to have the same thermal properties;

(iii) the tube wall is assumed to be of semi-infinite thickness.

For a step change in temperature with the properties and geometry of the experiments, approximation (i) leads to an under-estimate of the heat flux by about 10%, but approximation (ii) leads to a small over-estimate because the ratio of the values of $(\rho ck)^{1/2}$ for water and borosilicate glass is 1.1. Approximation (ii) will be removed later, in Section 7. Approximation (iii) is satisfactory because bubble growth times are such that $(\alpha t)^{1/2}$ is of order 0.2 mm, compared to the wall thickness of 0.5 mm or 0.7 mm. The assumption of constant thickness and the approximations can be removed by direct numerical simulation of the temperature fields in elements of the film of increasing age, but only at the cost of significantly increased computational time. This may be necessary for fluids with much larger density ratios ρ_V/ρ_L. Using the approximations, the heat flux $q_C(z,t)$ to the interface at position z, first formed at time t_Z, is calculated by

$$q_C(z,t) = \frac{k_L}{\sqrt{\pi\alpha_L}}\left[\frac{T_0 - T_S(t_Z)}{\sqrt{t-t_Z}} - \int_{t_Z}^{t} \frac{\mathrm{d}T_S/\mathrm{d}\zeta}{\sqrt{t-\zeta}}\,\mathrm{d}\zeta\right]. \tag{7}$$

The heat fluxes to the hemispherical ends are assumed to be equal, $q_{H1} = q_{H2}$, and to remain constant at the value q_H given by Eq.(3) at the instant of confinement. This may be a reasonable approximation at small t, when the changes in $P(t)$ are small and the heat input to the ends determines the initial velocity. It will become inaccurate at larger t as local flow patterns develop at the nose of the bubble, but by then the main heat supply should be to the cylindrical mid-section.

4.3.2 Wall Shear Stress

For the initial calculations, the shear stress τ acting on the liquid column ahead of the bubble is calculated by the expression for fully-developed laminar flow:

$$\tau = \frac{4\mu_L U_L}{R}. \tag{8}$$

4.4 Equations for Constant Film Thickness

For constant film thickness δ the conservation equations are as follows.

Vapour Mass:

$$M = \pi \rho_V(P)(R-\delta)^2 \left[\frac{4}{3}(R-\delta) + Z\right]. \tag{9}$$

Energy:

$$h_{LV}\frac{\mathrm{d}M}{\mathrm{d}t} = 2\pi(R-\delta)\left[(R-\delta)(q_{H1}+q_{H2}) + \int_0^Z q_C(z)\,\mathrm{d}z\right]. \tag{10}$$

Liquid Continuity:

$$\frac{U_L}{U_B} = \frac{\mathrm{d}U_L/\mathrm{d}t}{\mathrm{d}U_B/\mathrm{d}t} = \left(1-\frac{\delta}{R}\right)^2, \tag{11}$$

where

$$U_B = \frac{\mathrm{d}Z}{\mathrm{d}t}, \quad \frac{\mathrm{d}U_B}{\mathrm{d}t} = \frac{\mathrm{d}^2Z}{\mathrm{d}t^2}. \tag{12}$$

Liquid Momentum:

$$P - P_A - \left[\frac{1+(1-\delta/R)^2}{1-\delta/R}\right]\frac{\sigma}{R} = (L-Z)\left[\rho_L\left\{g + (1-\delta/R)^2\frac{\mathrm{d}^2Z}{\mathrm{d}t^2}\right\} + \frac{2\tau}{R}\right]. \tag{13}$$

The above set of equations is equivalent to a third-order differential equation for any variable such as $Z(t)$, requiring three initial conditions. The length of the cylindrical section is taken to be zero at $t = 0$:

$$Z = 0 \quad \text{at} \quad t = 0. \tag{14}$$

The initial bubble velocity is calculated from the heat input through the hemispherical ends, assuming that the pressure, and therefore the vapour density, is nearly constant:

$$U_B = \frac{4q_H}{\rho_V h_{LV}} \quad \text{at} \quad t = 0. \tag{15}$$

The third initial condition is chosen to be

$$\frac{\mathrm{d}U_B}{\mathrm{d}t} = 0 \quad \text{at} \quad t = 0. \tag{16}$$

This is consistent with the experimental observation that the pressure is nearly constant initially, but it is not derived rigorously from a model for transition from unconfined to confined growth. Further consideration of the physical justification for this condition is required.

5 Simulations with Simple Assumptions

5.1 Solution of Equations

Equations (3)–(5), (7)–(16) were solved for $Z(t)$ and $P(t)$ by a first-order finite difference scheme with a time step of 5×10^{-5} s for specified values of the unconfined bubble growth factor C_B and the uniform film thickness δ. The numerical solution was validated at very small times by comparison with an analytical solution of the equations obtained as a power series in $t^{1/2}$. Representative parametric studies of the influence of C_B and δ, and also of the experimental uncertainty in the initial superheat, are shown in Fig.(7) for the experiment at a nominal superheat of 2.2 K in the 0.80 mm diameter tube. The simulations are for confined growth only, so their origin is taken to be 10 ms after the timing of bubble initiation in the experiments, to allow for the initial period of unconfined growth. By choosing appropriate combinations of values for the parameters, it is possible to match the experimental measurements of $Z(t)$ and $P(t)$ reasonably well during confined growth until the pressure approaches its maximum value. The data at later times, particularly the shape of the pressure pulse $P(t)$ at and beyond its maximum value, are always predicted poorly.

5.2 Influence of the Unconfined Bubble Growth Factor C_B

For values of the unconfined bubble growth factor C_B of order unity that are derived from the unconfined growth model, Eq.(1)–(3), the simulations predict two maxima in $P(t)$ of similar magnitude, Fig.(7b). The rise to the first maximum occurs very rapidly in about 5 ms. The pressure then falls, followed by a much slower rise to the second maximum, which occurs when the bubble is close to the open end of the tube. The final fall to atmospheric pressure then occurs very rapidly. The first maximum in P was not observed in the experiments, although the pressure measurement was fast enough to detect it, and the second maximum occurred much earlier in the progress of the bubble along the tube, so that the fall to atmospheric pressure was more gradual than in the simulations. As C_B is reduced, the magnitude of the first simulated maximum decreases, falling below 0.1 kPa (the lowest value detectable by the pressure transducer) for values of C_B less than 0.15. The reduction in C_B has negligible effect on the magnitude and shape of the second maximum in P, but shifts the entire $Z(t)$ and $P(t)$ plots to the right, Fig.(7a,b). For a change in C_B from 1.0 to 0.1, the time shift is nearly 50 ms, corresponding to a 50% increase in the time taken for the bubble to reach the end of the

tube.

C_B influences the simulation via the heat flux to the small area of the hemispherical ends of the bubble, Eq.(3), and the initial velocity, Eq.(15). Its significant influence on the simulated transit time is contrary to the intuitive expectation, expressed by Moriyama and Inoue [17] for their study of confined growth between parallel plates, that the method of initiating growth should not affect the later stages of growth driven by evaporation from the much larger area of the thin film. However, the following simple analytical model for growth at constant superheat T (i.e. negligible change in pressure) in a tube or (with minor modifications) between parallel plates provides an example in which the heat input to the small part of the interface bridging the gap between the walls strongly influences the entire period of growth. Suppose that the cylindrical length Z of the bubble is surrounded by a thin liquid film of uniform thickness with a linear temperature profile, equivalent to a constant heat transfer coefficient h, and that there is a decreasing heat transfer coefficient $h_0 \mathrm{e}^{-\lambda t}$ on the hemispherical ends. Then

$$\pi R^2 \rho_V h_{LV} \frac{\mathrm{d}Z}{\mathrm{d}t} = 2\pi RThZ + 4\pi R^2 T h_0 \mathrm{e}^{-\lambda t}, \tag{17}$$

and hence

$$Z = \frac{4Th_0}{\rho_V h_{LV}} \frac{(\mathrm{e}^{Kt} - \mathrm{e}^{-\lambda t})}{(K+\lambda)}, \quad \text{where} \quad K = \frac{2hT}{R\rho_V h_{LV}}. \tag{18}$$

In this simple case, the rate of growth at all times is proportional to the initial heat flux Th_0 on the hemispherical ends. Therefore confined bubble growth under more general conditions may also be sensitive to the precise conditions during the approach to confinement, which would have implications for reproducibility in the present experiments, in which nucleation might have occurred at different positions on the triggering wire, and for the regularity of bubble production in confined-bubble flow boiling in micro-channels. The process of bubble growth from nucleation to confinement requires more detailed study, e.g. by two-dimensional or three-dimensional CFD simulation, as in [13, 14], to explain the apparent requirement for an initial heat input at the start of confined growth that is an order of magnitude smaller than expected from Eq.(3). Meanwhile, the one-dimensional simulations in the remainder of this paper are performed with $C_B = 0.15$, in order to reduce the unphysical first maximum in $P(t)$ to negligible magnitude.

5.3 Influence of Film Thickness δ

Increasing the film thickness δ increases the rate of growth, without a time shift near the origin, and has negligible effect on the amplitude of the maximum pressure, Fig.(7c,d). The thickness has no effect on the heat flux to the bubble interface, because of the assumption that the film and the wall together form a semi-infinite slab with uniform properties. A large difference in properties should enhance the experimental sensitivity to film thickness, as will be shown in Section 7, but the choice of wall material was restricted by the requirement for transparency, in order to observe bubble growth. Film thickness that is not negligible compared to the tube radius has interacting influences in the simulation by changing the surface area for heat transfer, the volume of the bubble, and the ratio of the velocities of the bubble and the liquid column.

5.4 Influence of Experimental Uncertainty in Initial Superheat

The sensitivity to the experimental uncertainty in the initial superheat, as seen in Fig.(7e,f), is unsurprising. Increasing superheat increases the rate of growth and the amplitude of the pressure changes.

5.5 Estimated Values of Film Thickness

Based on the above sensitivity studies, the values of the film thickness δ in Table 1 were chosen for each of the five experimental runs to obtain reasonable simulations of $Z(t)$ and $P(t)$ during confined bubble growth up to the occurrence of maximum pressure, Fig.(8). In four cases, it was necessary to increase the superheat to a value at or near the upper limit of experimental uncertainty. More accurate control and measurement of temperature relative to the saturation temperature at atmospheric pressure will be required in future experiments at low superheats. The choice of film thickness ranged between 0.030 mm and 0.080 mm, increasing with superheat and tube diameter. There was no value that could be chosen to produce even an approximate prediction of the position along the channel at which the maximum pressure occurred and the subsequent rate of decrease in pressure. Features of the model that may affect the poor simulation of the later stages of expulsion of liquid from the tube are considered in Sections 6 and 7.

6 Improvements to Flow Modelling

6.1 Investigation of Shear Stress Modelling Assumption using the Full Set of Equations

The equations employed in Section 5 involve assumptions that are unlikely to be good approximations to the physical system. For example, the wall shear stress is modelled with Eq.(8) for fully-developed steady laminar flow even though, in every run, the liquid column was accelerated to Reynolds numbers $Re_L = 2\rho_L U_L R/\mu_L$ well above the conventional value of 2000 for transition to turbulent flow. Whether transition actually occurred in the experiments or was delayed by the high acceleration is not known. The notional transition point does not appear to correspond to any particular feature in the experimental growth curves in Fig.(3). A liquid Reynolds number of $Re_L = 2000$ corresponds to a bubble velocity U_B somewhat higher than 1.2 m/s in the 0.48 mm tube or 0.7 m/s in the 0.80 mm tube, the uncertainty depending on the value assumed for δ in Eq.(11). (The bubble Reynolds number is defined as $Re_B = \rho_L U_B R/\mu_L$, using the tube radius as characteristic length for consistency with the published correlations for δ discussed later in this Section.) The simulation was also run with a standard correlation for the shear stress in steady turbulent flow

$$\tau = 0.020 \left(\frac{\mu_L \rho_L^4}{R} \right)^{1/5} \left[\left(1 - \frac{\delta}{R} \right)^2 U_B \right]^{9/5}, \tag{19}$$

applied either with a step change at $Re_L = 2000$ or with a smooth change at $Re_L = 1500$. Apart from a small, rapidly-damped oscillation at the step change, the two procedures produce the same prediction of the pressure pulse $P(t)$, Fig.(9). The turbulent shear stress causes only small increases in the maximum pressure and in the time taken for the bubble to reach the end of the tube, suggesting that that the modelling of wall shear stress is not a critical issue. The disadvantage of this approach is that a particular aspect of a nonlinear model is being examined by solving a large set of equations that may contain other dubious features affecting both the thermal and dynamical modelling, such as the assumption of constant film thickness.

6.2 Investigation of Shear Stress Modelling Assumption using the Momentum and Continuity Equations

6.2.1 Method

An alternative method of testing the flow modelling assumptions is to use the experimental data for the bubble length $Z(t)$ and the pressure $P(t)$ as known inputs (except for experimental

error) to the continuity and momentum equations Eqs.(11)–(13). The momentum equation (13) then has film thickness $\delta(t)$ and wall shear stress $\tau(t)$ as the only unknowns, but an assumption must be made about one in order to calculate the other. Both quantities have been studied extensively in adiabatic systems, but rarely for the property range and conditions of high acceleration relevant to flow boiling in microchannels.

6.2.2 Correlations for Film Thickness

For fully-developed, steady, adiabatic flow of long bubbles in tubes that are small enough for gravity to have a negligible effect, the non-dimensional film thickness δ/R after the film comes to rest relative to the wall is a function of the capillary number $Ca = \mu_L U_B/\sigma$ and the non-dimensional tube radius $F = \rho_L \sigma R/{\mu_L}^2$. (Note that the bubble Reynolds number is related to Ca and F by $Re_B = CaF$.) For flows with negligible inertia, there are well-known analytical expressions and experimental correlations, e.g. by Taylor [23] for $Ca \ll 1$

$$\frac{\delta}{R} = 1.34\, Ca^{2/3}, \tag{20}$$

extended by Aussillous and Quéré [24] to $Ca < 2.5$, but still with $CaF \ll 1$, to

$$\frac{\delta}{R} = \frac{1.34\, Ca^{2/3}}{1 + 3.35\, Ca^{2/3}}. \tag{21}$$

There is little information for the conditions of the present study, with $Ca < 10^{-2}$ and F of order 3×10^5 so that the Reynolds numbers span the laminar-turbulent transition. Some limited experimental data in [24] for $Re_B < 10^3$ and an extended asymptotic analysis by de Ryck [25] for laminar flows with weak inertia show that the inertial effects in steady flow cause a significant increase in film thickness beyond a critical value of Ca^* given by

$$Ca^* = 28\, F^{-3/4} \tag{22}$$

derived from Eq.(10) and Fig.(5) of [24]. There is even less information about film thickness in flows that are developing either in space or time. Aussillous and Quéré [24] found that the film deposited from a very short liquid slug of length S in steady flow was limited to the thickness of the axially developing boundary layer, given by

$$\delta = O\left(\frac{\mu_L S}{\rho_L U_B}\right)^{1/2}, \tag{23}$$

similar in form to the Cooper and Lloyd [26] estimate for the thickness of the microlayer under an unconfined bubble after growth time t_g:

$$\delta = C_M \left(\frac{\mu_L t_g}{\rho_L} \right)^{1/2}, \tag{24}$$

with constant of proportionality C_M in the range 0.4–0.8. There have been only a few published numerical studies of the accelerating motion of bubbles confined in tubes, all for viscous liquids at large Ca irrelevant to boiling.

Moriyama and Inoue [17] identified two regimes for film formation in their experimental study of the unsteady growth of cylindrical bubbles in the low-viscosity fluid R113 between parallel plates with gaps of 0.1–0.4 mm, corresponding to values of F in the high range 4.7×10^3 – 1.9×10^4. The bubbles reached radial velocities U_B of up to 4 m/s, corresponding to a maximum instantaneous capillary numbers of 0.13, and accelerations $\dot{U}_B$ of up to 2000 m/s^2, corresponding to a maximum Bond number of 0.5, where the Bond number Bo is defined by

$$Bo = \frac{\rho_L R^2 \dot{U}_B}{\sigma}. \tag{25}$$

The definitions and correlations in [17] have been rewritten here with the gap half-width R as the characteristic length for consistency with the convention used in [24, 25]. Noting that the bubble radius $Z \propto t^2$ approximately, Moriyama and Inoue calculated the approximately constant acceleration $\dot{U}_B$ from U_B/t_g and redefined the Bond number as

$$Bo_{MI} = \frac{\rho_L R^2 U_B}{\sigma t_g}. \tag{26}$$

More accurately, their data followed $Z \propto t^n$, with n varying between 1.3 and 2.1 in different runs, so the substitution should have been $(n-1)U_B/t_g$ and the two definitions of the Bond number could differ in some runs by a factor of 3. Their correlations for the two regimes are

$$\frac{\delta}{R} = \begin{cases} 0.14\, Ca^{0.41} & \text{for} \quad Bo_{MI} \le 0.5, \\ 0.11 \left[\dfrac{1}{R} \left(\dfrac{\mu_L t_g}{\rho_L} \right)^{1/2} \right]^{0.84} & \text{for} \quad Bo_{MI} > 0.5. \end{cases} \tag{27}$$

For small Bo_{MI}, the dependence of δ/R only on Ca suggests that the steady-flow correlation with negligible inertia should apply but, as noted by Moriyama and Inoue [17], their correlation gives values about three times smaller than the accepted correlation in Eq.(20) for the range of conditions in their study. They suggested that this might be because this range lay outside

the range of validity of Eq.(20), but the later steady-flow studies in [24, 25] lead to estimates of δ/R for these conditions that are increased, rather than decreased, compared to Eq.(20). The steady-flow correlations presuppose a fully-developed parabolic velocity profile in the liquid displaced by the bubble. For large Bo_{MI}, the correlation in Eq.(26) is rather similar to the expressions in Eqs.(23, 24) for liquid flow with a velocity boundary layer ahead of the bubble with thickness developing with distance or time, but again predicts values that are about three times smaller. Although the conditions of the studies are not the same, the discrepancy raises a concern that the correlation of Moriyama and Inoue [17] may significantly underpredict film thickness. One possibility that is difficult to test retrospectively is that the measured times for progressive dryout of the film, from which its thickness was inferred by a model for evaporation, might have been reduced by movement of the triple contact line under the influence of capillary forces generated by a finite contact angle. Retraction of the film at a velocity of 5–10% of the bubble velocity could account for the measured times to dryout.

Taha [27] used the commercial CFD code FLUENT to perform a two-dimensional simulation of the adiabatic expulsion of liquid from a capillary tube by application of a gas pressure, so that thermal modelling was not involved. A constant pressure difference of 4 kPa was applied to water at 100°C in a 8 mm long tube with 0.4 mm radius, for which $F = 2.8 \times 10^5$. The conditions are somewhat similar to those for the growing vapour bubbles in the experiments described in Section 2, except that the liquid column is much shorter and the bubble therefore accelerates more rapidly, giving larger values of Bo and Bo_{MI}. The flow in the liquid column was assumed to remain laminar. The starting condition for the simulation was a plane interface pinned at the sharp entrance to the tube. As the interface became curved, the triple contact line began to move along the tube at a velocity dependent on the constant dynamic contact angle of 10° or 60° specified at the wall, developing the familiar moving capillary hump. The code provides only a crude approximation to the complicated physics in the microscopic contact zone. The developing shape of the confined bubble is shown in Fig.(10), with the radial scale expanded in the upper diagram to show details of the liquid film. At a contact angle of 10°, there was only a slow movement of the contact line. The nose of the bubble left behind a thin liquid film that became nearly stationary after a distance of 3 or 4 tube radii. This distance and the deposited thickness of the film increased as the bubble grew. At a contact angle of 60°, the contact line moved much more rapidly at a velocity that was comparable with

that of the bubble nose. The film was much shorter, so that the disturbances at the nose and the contact line interacted. The film was thicker and did not become stationary, so that the modelling assumptions in Section 4 would not be appropriate.

The values of stationary film thickness in the simulation for a contact angle of 10° at distances of $3R$ and $4R$ behind the bubble nose are compared with the correlations in Eqs.(21, 24) in Table 2. The rapid variation in flow conditions leads to the uncertainty about exactly what film thickness to associate with a particular nose velocity so stagnant film models are not applicable to bubbles with lengths less than $4R$. The steady-flow correlation of Aussillous and Quéré, Eq.(21), and the transient correlation Eq.(24) with $C_M = 0.8$ are both in approximate agreement with the simulation. There is too much uncertainty in the very limited evidence to test the proposal of Aussillous and Quéré that the correlation giving the lower value of film thickness should be used. The capillary numbers in the simulation are higher than the threshold value Ca^*, given by Eq.(22), for an increase in the thickness due to steady-flow inertial effects, but there is at present no guide to the magnitude of the increase for this combination of low Ca and large F. The correlations of Moriyama and Inoue, Eq.(27), predict much lower values for film thickness that are in poor agreement with this particular simulation of transient growth, Table 2, just as they are with Eqs.(21, 24) for the particular experimental conditions of [17].

Thome et al. [15, 16] modified the Moriyama and Inoue correlations by introducing a factor 3 in the expression for the diffusion layer thickness and a further correction factor C_{δ_0} that was assigned values between 0.34 and 1.23 to match heat transfer experiments with various refrigerants and a value of 0.29 for general use. They redefined the bubble growth time used to calculate the acceleration in the Bond number by $t_g = 2R/U_B$ and used an interpolating procedure to give a smooth transition between the Moriyama and Inoue correlations for low and high Bo. Their correlation, converted to tube radius R as the characteristic length, is

$$\frac{\delta}{2R} = C_{\delta_0}\left[3\left(\frac{\mu_L}{2\rho_L R U_B}\right)^{1/2}\right]^{0.84}\left[\left\{0.07\left(\frac{2\rho_L R U_B^2}{\sigma}\right)^{0.41}\right\}^{-8} + 0.1^{-8}\right]^{-1/8}. \qquad (28)$$

By assuming $C_{\delta_0} = 1$ and making small approximations as in [17], e.g. neglecting the difference between exponents of 0.41 and 0.42, this may be recast in a convenient form for comparison with the other correlations:

$$\frac{\delta}{R} = \begin{cases} 0.35\,Ca^{0.42} & \text{for} \quad Ca < F^{-1/2} \quad \text{approximately,} \\ 0.38\,Re^{-0.42} = 0.38(CaF)^{-0.42} & \text{for} \quad Ca > F^{-1/2} \quad \text{approximately,} \end{cases} \qquad (29)$$

The modifications have eliminated the influence of bubble growth time, as used in [17], and of boundary conditions ahead of the bubble, as discussed in [24]. The correlations should therefore apply to the same steady flow conditions as Eqs.(20, 21). With $C_{\delta_0} = 1$, the predictions of film thickness are not greatly different for the range $10^{-3} < Ca < 10^{-2}$ but Eq.(29) predicts an entirely different behaviour for the condition of increasing bubble velocity in a tube of fixed radius, i.e. that the film thickness reaches a maximum value and then decreases, which appears to be inconsistent with the available experimental evidence for steady flow. It is also inconsistent with the trend and values in the transient simulation in Fig.(10), Table 2.

It appears that there is at present no better guide to film thickness under transient conditions than the correlation for steady, laminar flow, Eq.(21), with the proviso that it may underpredict the thickness at large values of F and overpredict for those transient conditions for which Eq.(21) predicts a lower value. However, the values of film thickness chosen in Section 5 to optimize the fit of the model to the experimental data up to the time of maximum pressure are 3 to 5 times larger than the values calculated from Eq.(21) for the measured velocities at the maximum pressure, Table 1, and the other correlations considered in this Section predict even smaller values for the film thickness. The large discrepancy shows that further studies are required of transient film formation over the range of conditions relevant to flow boiling in microchannels. It should be possible to obtain valuable information from experiments and numerical simulations under adiabatic conditions, which are less difficult to perform than studies involving phase change.

6.2.3 Deduction of Wall Shear Stress

In the absence of a reliable correlation for δ/R for the conditions of these experiments, shear stresses were calculated from the momentum equation Eq.(13) for two fixed values of δ in the range estimated in Section 5 and for $\delta(t)$ calculated with the steady flow correlations Eqs.(20, 21). The film thickness affects the ratio of the liquid and bubble velocities and accelerations through Eq.(11). Values of the bubble velocity $U_B = \mathrm{d}Z/\mathrm{d}t$ and acceleration $\mathrm{d}U_B/\mathrm{d}t = \mathrm{d}^2Z/\mathrm{d}t^2$ were obtained by differentiating a cubic polynomial fitted to each growth curve in Fig.(3). This procedure is open to the same criticisms made of [17] in Section 6.2.2. It smoothed out some of what might have been experimental noise or genuine fluctuations and differentiation might then cause errors in the large inertial term that was subtracted from the

total pressure drop to give the frictional resistance.

The calculated shear stresses are plotted against the liquid velocity U_L in Fig.(11) for one run in each size of tube. The shear stresses for steady laminar and turbulent flow, which are expected to be lower bounds for the shear stresses in transient flows with monotonically increasing velocity, are also shown for reference. All the graphs have the same general shape, displaced towards higher values of U_L for correlations that predict lower values of δ. At small U_L, small values of δ lead to values of τ lying below the line for steady laminar flow and even going negative: this may be due to errors in measuring the small initial values of U_B or underestimation of the film thickness during the transition to confined growth. The broad plateau in τ is unexpected. In both of the runs in Fig.(11), it commences close to the nominal laminar-turbulent transition and also the peak of the pressure pulse, where the raw data indicate irregularities in the acceleration that have been smoothed out in this analysis. Beyond the plateau, the calculated shear stresses all lie below the line for steady turbulent flow. In some cases they are below the extrapolated line for laminar flow, which should be a lower bound, so the estimated film thickness must be too small, even if turbulence has been completely suppressed in the accelerating flow.

The unexplained features of Fig.(11) confirm that further investigation is required of both film thickness and wall shear stress in bubble-driven flows accelerating through the laminar-turbulent transition.

7 Improvements to Thermal Modelling

7.1 Effect of Wall Thermal Properties

Retaining the assumption of constant film thickness, the effect of differences between the thermal properties of the fluid and of the wall was assessed by replacing Eq.(7) by the expression for transient conduction in a layer of finite thickness δ on a semi-infinite substrate, based on Carslaw and Jaeger [28],

$$q_C(z,t) = \frac{k_L\left[T_0 - T_S(t_Z)\right]}{\sqrt{\pi\alpha_L(t-t_Z)}}\left[1 + 2\sum_{n=1}^{\infty}\beta^n \exp\left(-\frac{n^2\delta^2}{\alpha_L(t-t_Z)}\right)\right] - \int_{t_Z}^{t}\frac{k_L \mathrm{d}T_S/\mathrm{d}\zeta}{\sqrt{\pi\alpha_L(t-\zeta)}}\left[1 + 2\sum_{n=1}^{\infty}\beta^n \exp\left(-\frac{n^2\delta^2}{\alpha_L(t-\zeta)}\right)\right]\mathrm{d}\zeta, \tag{30}$$

where

$$\beta = \frac{\phi - 1}{\phi + 1}, \quad \phi = \left(\frac{k_W \rho_W c_W}{k_L \rho_L c_L} \right)^{1/2}. \tag{31}$$

Simulations for water in tubes of borosilicate glass, stainless steel, silicon or copper are presented in Fig.(12) for one experimental run in each tube of radius 0.24 mm and 0.40 mm. For all these materials, simulations with the optimized values of film thickness of 0.030 mm and 0.080 mm respectively are indistinguishable from the original single layer model using the properties of water (thick black line). This suggests that most of the heat driving bubble growth is conducted from within the thick liquid film, before the thermal diffusion layer has penetrated to the wall. There is no effect on the poor performance of the simulation of the pressure pulse beyond the occurrence of maximum pressure. Simulations with the film thickness reduced by an order of magnitude to 0.003 mm and 0.008 mm respectively fit the experimental data less well up to the time of maximum pressure. The thinner films cause sensitivity to the wall properties. The single semi-infinite layer model is still a good approximation for water-glass. The simulations for water on walls with thermal conductivities in the range 17 W/mK (stainless steel) to 400 W/mK (copper) form a fairly close group with predicted bubble growth rate about twice that on glass.

7.2 Effect of Liquid Film Roll-Up

The changes to the basic model that have been discussed so far have failed to improve its poor simulation of the later stages of the pressure pulse. The insensitivity in this respect to the submodel for wall shear stress, demonstrated in Fig.(9), suggests that some fundamental change is required in the thermal model that will produce a large reduction in the rate of evaporation after the experimentally measured maximum pressure. It is not known how transition from laminar to turbulent flow in the liquid column would affect film thickness, but it might be expected to *increase* heat transfer in the vicinity of the bubble nose.

A key feature of the model is that the liquid film becomes static a short distance behind the nose of the bubble and remains in place over its entire length. Reduction in the film length by evaporation to dryness would reduce subsequent evaporation, as in the flow boiling model in [15], but is estimated from Eq.(6) to be insignificant for the conditions of these experiments. An entirely separate mechanism for reduction of the area for evaporation is "roll-up" of the liquid film under the influence of the capillary pressure gradient caused by a large contact angle,

suggested in Section 6.2.2 as a possible influence on the experiments in [17] and illustrated by the adiabatic CFD simulation in Fig.(10), which would reduce the area of film driving bubble growth by evaporation. This effect of film roll-up was reproduced approximately in the one-dimensional simulation of vapour bubble growth by computing the heat input only over a fixed length behind the nose of the bubble, implemented by adjusting the lower limit of integration in Eq.(10). (No allowance was made for intensive evaporation at the triple contact line). Progressive reductions in this length caused the maximum pressure to occur earlier, Fig.(13). The change in gradient immediately after the maximum was sharper in the tube of larger radius, but the very last stage of the decrease to atmospheric pressure was still faster than occurred in the experiments. Similar effects occurred in simulations with the two-layer model using a sub-optimum film thickness, Fig.(14).

There is no direct evidence from the experiments that film roll-up actually occurred: a video camera field large enough to track the nose of the bubble over a long distance led to low resolution of flow details behind the nose. The prerequisites for this mechanism are the formation of a triple contact line with a relatively large contact angle, much greater than 10°. The cleaning procedure adopted in the experiments was intended to produce a well-wetted wall but *in situ* contact angle measurements were not made: they should be included in future experiments. A contact angle can only form after the liquid film has dried out somewhere along its length, perhaps by evaporation at a locally thin region, and motion of the contact line must be initiated within the measured time for the pressure to reach its maximum value, taken from Fig.(3), if roll-up of the film is to influence the subsequent growth. The time t_E for a liquid film of thickness δ_0 to evaporate to dryness is sensitive to the wall thermal conditions. The heat transferred to the liquid-vapour interface in the time interval $0 < t < t_E$ is estimated from the single-layer transient conduction equation appropriate to the conditions of the experiments, with the time-varying temperature difference approximated by an average value $\bar{T}$ which is less than the initial superheat T_0. Equating this heat to the enthalpy of evaporation of the film,

$$2\bar{T}\left(\frac{\rho c k t_E}{\pi}\right)^{1/2} \simeq \rho h_{LV} \delta_0. \tag{32}$$

Substituting the measured times to maximum pressure for the five runs and mean temperature differences of half the initial superheat leads to estimates of the maximum film thickness that could evaporate to dryness in the time available of 0.2–0.4 μm, much smaller than the optimized uniform film thickness values of 30–80 μm. The most favourable conditions for the formation

of very thin films would be close to the origin, during the transition to confined growth, and it has been noted in Section 5.2 that there are uncertainties in modelling this process. For thin films on walls of relatively high thermal conductivity, a model assuming linear temperature profiles in the liquid and an isothermal wall, for which

$$t_E = O\left(\frac{{\delta_0}^2 \rho_L h_{LV}}{2k_L T}\right), \tag{33}$$

which would lead to much higher estimates of the maximum film thickness for evaporation to dryness.

Annular liquid films are also subject to a Rayleigh instability with fastest growing wavelength $8.9R$ [29] and time constant t_R given by

$$t_R = \frac{12\mu_L R^4}{\sigma\delta^3}. \tag{34}$$

Setting t_R equal to the time of the maximum pressure leads to estimates of the *minimum* film thickness near the origin of the bubble that would become unstable of 14–18 μm for runs in the 0.24 mm radius tube and 25–28 μm in the 0.40 mm radius tube. These values are less than the optimized values of 30 μm and 80 μm, respectively, so this appears to be a possible mechanism for the creation of a dry spot if the optimized values are indeed approximately correct.

While it is uncertain whether roll-up of the liquid film was initiated in these experiments, the postulated mechanism is consistent with the evidence of a region of deteriorated heat transfer propagating with confined bubbles in flow boiling experiments in channels of rectangular cross-section 2 mm $\times$ 1 mm [10]. In that geometry, the film would also have been subject to transverse roll-up towards the corners due to capillary forces.

7.3 Other Issues

The initial heat flux to the newly-formed interface at the front of the bubble, at present assumed to be infinite in Eqs.(7, 30), is actually finite and dependent on the convective conditions in the region of formation of the liquid film at the nose of the bubble. This issue requires further attention.

In confined-bubble flow boiling, heat transfer in the liquid film would inherit an initial temperature profile dependent on heat transfer in the liquid plug ahead of the bubble, as modelled approximately for the microlayer under an unconfined sliding bubble in [30].

8 Conclusions

1. A method has been described for the experimental investigation of the triggered growth of a single vapour bubble in uniformly superheated water in a capillary tube. The observations under simplified conditions were used to examine assumptions relevant to one-dimensional models for flow boiling heat transfer in microchannels. The experiment employed inexpensive instrumentation but was difficult to implement. Desirable improvements in the technique were noted.

2. The growth of a bubble created a pressure pulse that reached a maximum value and then gradually declined as the bubble approached the end of the tube. The decrease in superheat available to drive bubble growth was a large fraction of the initial superheat. The thermal consequences of pressure variations caused by bubble growth should be incorporated in models for flow boiling in microchannels.

3. There is at present no reliable correlation to predict the thickness of the liquid film round confined bubbles for the particular conditions of high Reynolds number, high Bond number (high acceleration) and low capillary number with transition from laminar to turbulent flow, all relevant to flow boiling in microchannels.

4. A one-dimensional model employing conventional flow correlations and assuming transient conduction in the liquid film and the tube wall was unable to simulate the timing of the maximum pressure and its subsequent rate of decline. Values for film thickness deduced by matching the model to the experimental measurements up to the time of maximum pressure were several times larger than the predictions of the best available correlation.

5. A hypothesis was presented that the bubble growth rate was reduced by roll-up of the thin liquid film by movement of the contact line due to capillary forces, rather than evaporation to dryness.

6. According to the model, the initial growth rate of the bubble exerts a lasting influence on its subsequent growth. The transition from unconfined to confined growth requires more study.

Acknowledgements

This work was supported by the Engineering and Physical Sciences Research Council under Research Grant GR/R74468. D.S.W. received support from the K.C. Wong Education Foundation, the Henry Lester Trust, Wing YP Brothers, the British Council, and Lincoln College, Oxford. All the authors are grateful to Dr Taha Taha for permission to use Fig.(10).

Nomenclature

$Bo = \rho_L R^2 \dot{U}_B / \sigma$	Bond number
$Bo_{MI} = \rho_L R^2 U_B / \sigma t_g$	Bond number used in [17]
$Ca = \mu_L U_B / \sigma$	capillary number
C_B	unconfined bubble growth factor
C_M	constant of proportionality in Eq.(24)
C_{δ_0}	correction factor used in [15]
c	specific heat, J/kg K
$F = \rho_L \sigma R / {\mu_L}^2$	non-dimensional tube radius
f	group formation frequency used in [15]
g	gravitational acceleration, m/s^2
h	heat transfer coefficient, W/m^2 K
h_{LV}	enthalpy of evaporation, J/kg
$Ja = \rho_L c_L (T_0 - T_{S0}) / \rho_V h_{LV}$	Jakob number
$K = 2hT / R\rho_V h_{LV}$	non-dimensional group appearing in Eq.(18)
k	thermal conductivity, W/m K
L	tube length, m
M	mass of vapour
P	pressure, Pa
q	heat flux, W/m^2
$Re_B = \rho_L U_B R / \mu_L$	bubble Reynolds number
$Re_L = 2\rho_L U_L R / \mu_L$	liquid Reynolds number
R	tube radius, gap half-width, m
S	liquid slug length, m
T	temperature, K
$\bar{T}$	average value of T in Eq.(32), K
t	time, s
t_g	bubble growth time, s
t_0	confinement time, s
U_B	bubble velocity, m/s
U_L	liquid velocity, m/s
$\dot{U}_B$	bubble acceleration, m/s^2
Z	bubble length, m
z	axial coordinate
α	thermal diffusivity, m^2/s
Δ	average change in film thickness, m
δ	film thickness, m
λ	exponent appearing in Eqs.(17, 18), 1/s
μ	viscosity, Pa s
ρ	density, kg/m^3
σ	surface tension, N/m
τ	shear stress, Pa

Subscripts

A	atmospheric
B	bubble
C	cylindrical region
E	evaporation
H	hemispherical end
L	liquid
R	Rayleigh
S	saturation
V	vapour
W	wall
0	initial
min	minimum

References

[1] S.G. Kandlikar, High flux heat removal with microchannels - a roadmap of challenges and opportunities, in: Proceedings of 3rd International Conference on Microchannels and Minichannels, Toronto, 2005. Paper 75086.

[2] S. Lin, P.A. Kew and K. Cornwell, Evaporation heat transfer and pressure drop of refrigerant R-134a in a small pipe, International Journal of Refrigeration 24 (2001) 51–56.

[3] Y. Yan and D.B.R. Kenning, Pressure and temperature fluctuations during boiling in a narrow channel, in: Eurotherm 62: Heat Transfer in Condensation and Evaporation, Grenoble, 1998, pp. 107–117.

[4] D.B.R. Kenning and Y. Yan, Saturated flow boiling of water in a narrow channel: experimental investigation of local phenomena, IChemE Transactions A, Chemical Engineering Research and Design 79 (2001) 425–436.

[5] P.A. Kew and K. Cornwell, On pressure fluctuations during boiling in narrow channels, in: Proceedings of 2nd European Thermal Sciences and 14th UIT National Heat Transfer Conference, Rome, 1996, pp. 1323–1327.

[6] D. Brutin, F. Topin and L. Tadrist, Experimental study of the unsteady convective boiling in heated minichannels, International Journal of Heat Transfer 46 (2003) 2957–2965.

[7] D. Brutin and L. Tadrist, Pressure drop and heat transfer analysis of flow boiling in a minichannel; influence of the inlet condition on two-phase flow stability, International Journal of Heat and Mass Transfer 47 (2004) 2365–2377.

[8] A.E. Bergles and S.G. Kandlikar, On the nature of critical heat flux in microchannels, Journal of Heat Transfer 127 (2005) 101–107.

[9] S.G. Kandlikar, D.A. Willistein and J. Borelli, Experimental evaluation of pressure drop elements and fabricated nucleation sites for stabilizing flow boiling in minichannels and microchannels, in: Proceedings of 3rd International Conference on Microchannels and Minichannels, Toronto, 2005. Paper 75197.

[10] D.S. Wen, D.B.R. Kenning and Y. Yan, Flow boiling of water in a narrow vertical channel at low mass flux: observations of local phenomena, in: Proceedings of 12th International Heat Transfer Conference, Grenoble, 2002, pp. 773–778.

[11] L. Zhang, K.E. Goodson and T.W. Kenny, *Silicon Microchannel Heat Sinks, Theories and Phenomena*, Springer, Berlin, 2004, chapters 5–7.

[12] L. Zhang, E.N. Wang, K.E. Goodson and T.W. Kenny, Phase change phenomena in silicon microchannels, International Journal of Heat and Mass Transfer 48 (2005) 1572–1582.

[13] A. Mukherjee and S.G. Kandlikar, Numerical simulation of growth of a vapor bubble during flow boiling of water in a microchannel, in: Proceedings of 2nd International Conference on Microchannels and Minichannels, Rochester, 2004. Paper 2382.

[14] A. Mukherjee and S.G. Kandlikar, Numerical study of the effect of inlet constriction on bubble growth during flow boiling in microchannels, in: Proceedings of 3rd International Conference on Microchannels and Minichannels, Toronto, 2005. Paper 75143.

[15] J.R. Thome, V. Dupont and A.M. Jacobi, Heat transfer model for evaporation in microchannels. Part I: presentation of the model, International Journal of Heat and Mass Transfer 47 (2004) 3375–3385.

[16] V. Dupont, J.R. Thome and A.M. Jacobi, Heat transfer model for evaporation in microchannels. Part II: comparison with the database, International Journal of Heat and Mass Transfer 47 (2004) 3387–3401.

[17] K. Moriyama and A. Inoue, Thickness of the liquid film formed by a growing bubble in a narrow gap between two horizontal plates, Journal of Heat Transfer 118 (1996) 1223–1230.

[18] M.B. Shafii, A. Faghri and Y. Zhang, Thermal modeling of unlooped and looped pulsating heat pipes, Journal of Heat Transfer 123 (2001) 1159-1172.

[19] B. Holley and A. Faghri, Analysis of pulsating heat pipe with capillary wick and varying channel diameter, International Journal of Heat and Mass Transfer 48 (2005) 2635–2651.

[20] R.I. Eddington and D.B.R. Kenning, The effect of contact angle on bubble nucleation, International Journal of Heat and Mass Transfer 22 (1979) 1231–1236.

[21] M.S. Plesset and S.A. Zwick, The growth of a vapor bubble in superheated liquid, Journal of Applied Physics 25 (1954) 493–501.

[22] H. Yuan, H.N. Oguz and A. Prosperetti, Growth and collapse of a vapour bubble in a small tube, International Journal of Heat and Mass Transfer 42 (1999) 3643–3657.

[23] G.I. Taylor, Deposition of viscous fluid on the wall of a tube, Journal of Fluid Mechanics 10 (1961) 161–165.

[24] P. Aussillous and D. Quéré, Quick deposition of a fluid on the wall of a tube, Physics of Fluids 12 (2000) 2367–2371.

[25] A. de Ryck, The effect of weak inertia on the emptying of a tube, Physics of Fluids 14 (2002) 2102–2108 and 4100.

[26] M.G. Cooper and A.J.P. Lloyd, The microlayer in nucleate boiling, International Journal of Heat and Mass Transfer 12 (1969) 895–913.

[27] T. Taha, private communication, 2005.

[28] H.S. Carslaw and J.C. Jaeger, *Conduction of Heat in Solids*, Clarendon Press, Oxford, 1957, chapter 12, p. 322.

[29] L.W. Schwartz, H.M. Princen and A.D. Kiss, On the motion of bubbles in capillary tubes, Journal of Fluid Mechanics 172 (1986) 259–275.

[30] D.B.R. Kenning, O.E. Bustnes and Y. Yan, Heat transfer to a sliding vapour bubble, Multiphase Science and Technology 14 (2002) 75–94.

List of Figure and Table captions.

Figure 1. Experimental apparatus.

Figure 2. Conditions prior to initiation of growth (a) without and (b) with prepressurization.

Figure 3. Data for pressure $P(t) - P_A$, bubble length $Z(t)$ and bubble velocity $U_B(t)$: (a) 0.48 mm tube; (b) 0.80 mm tube.

Figure 4. Dependence of maximum pressure on initial superheat and tube diameter.

Figure 5. Non-dimensional plot of pressure change versus bubble length for all runs.

Figure 6. Model for bubble growth.

Figure 7. Sensitivity of simulations to modelling parameters for run 0.80/2.2: (a), (b) C_B; (c), (d) δ; (e), (f) $\Delta T = T_0 - T_S(P_A)$.

Figure 8. Simulations with optimised parameters (Table 1).

Figure 9. Effect of laminar-turbulent transition on pressure pulse.

Figure 10. Effect of dynamic contact angle on expulsion of liquid from an 8 mm long tube of diameter 0.8 mm by a constant gas pressure, Taha [27].

Figure 11. Shear stress deduced from measured $P(t)$ and $Z(t)$ for different $\delta(U_L)$: (a) 0.48 mm tube; (b) 0.80 mm tube.

Figure 12. Simulations with various wall materials: (a) 0.48 mm tube with $\delta = 0.030$ mm (optimised value, thick black line for all materials) and $\delta = 0.003$ mm; (b) 0.80 mm tube with $\delta = 0.080$ mm (optimised value, thick black line for all materials) and $\delta = 0.008$ mm.

Figure 13. Effect of simulated film roll-up with various film lengths: (a) 0.48 mm tube with optimised film thickness $\delta = 0.030$ mm; (b) 0.80 mm tube with optimised film thickness $\delta = 0.080$ mm.

Figure 14. Simulations with various wall materials and film roll-up with film length 25 mm: (a) 0.48 mm tube with $\delta = 0.030$ mm (optimised value, thick black line for all materials) and $\delta = 0.003$ mm; (b) 0.80 mm tube with $\delta = 0.080$ mm (optimised value, thick black line for all materials) and $\delta = 0.008$ mm.

Table 1. Optimised modelling parameters and film thickness from the Aussillous and Quéré [24] correlation, Eq.(21).

Table 2. Comparison of a numerical simulation of an accelerating bubble driven by constant gas pressure with dynamic contact angle 10° as shown in Fig.(10) [27] with correlations for liquid film thickness by Aussillous and Quéré Eq.(21), Cooper and Lloyd Eq.(24), Moriyama and Inoue Eq.(27), and Thome et al. Eq.(29).

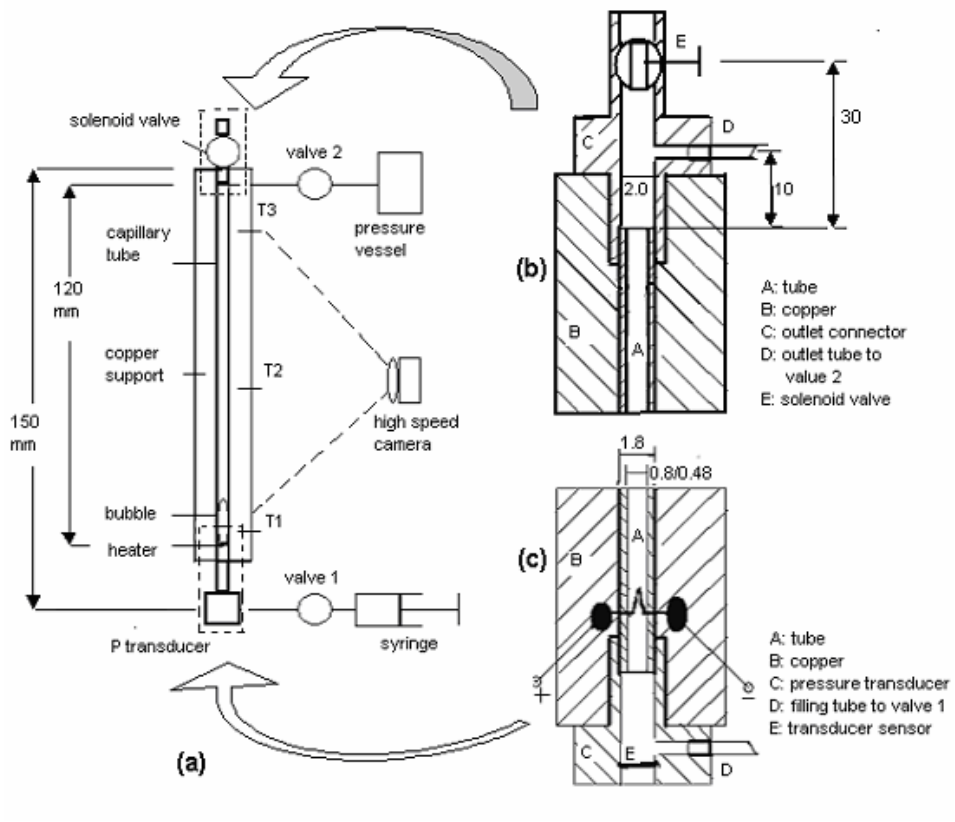
solenoid valve
valve 2
pressure vessel
T3
capillary tube
120 mm
copper support
T2
150 mm
high speed camera
bubble
T1
heater
valve 1
P transducer
syringe
(a)
(b)
E
C
D
30
10
2.0
B
A
A: tube
B: copper
C: outlet connector
D: outlet tube to value 2
E: solenoid valve
(c)
1.8
0.8/0.48
A
B
3
C
E
D
A: tube
B: copper
C: pressure transducer
D: filling tube to valve 1
E: transducer sensor

Figure 1:

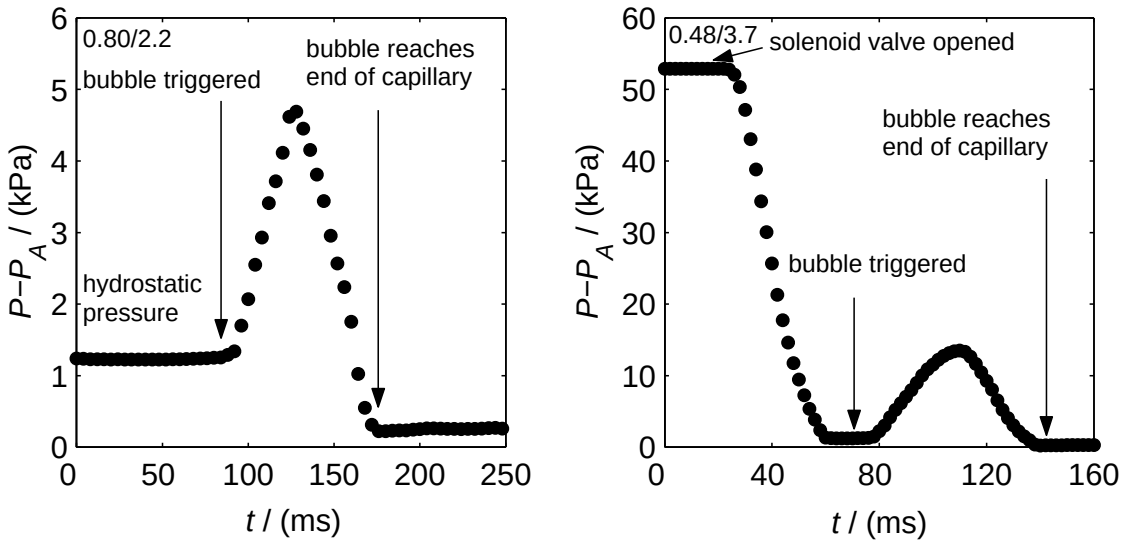

(a) no prepressurization

(b) with prepressurization

Figure 2:

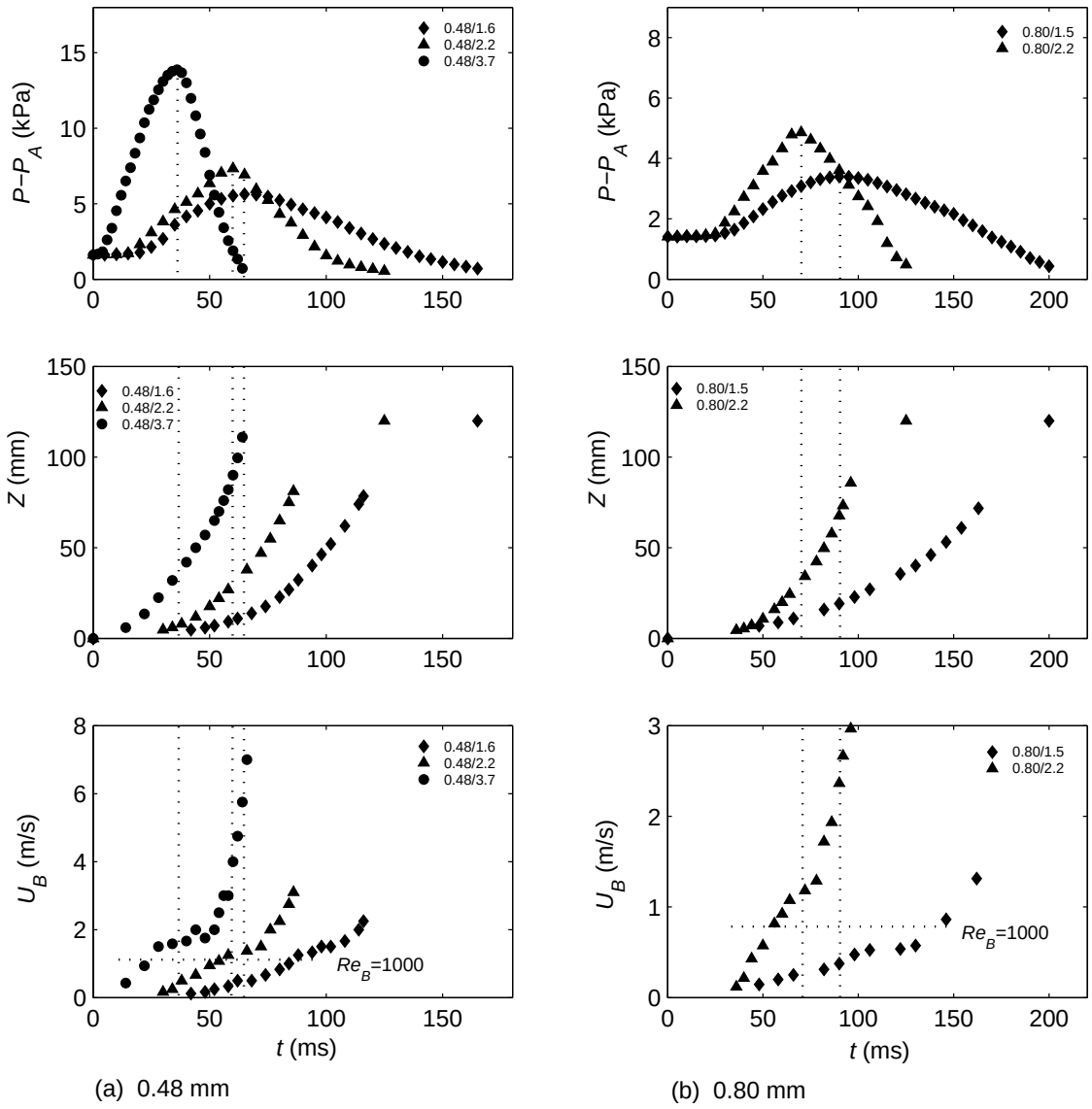
0.48/1.6
0.48/2.2
0.48/3.7
P–P_A (kPa)
Z (mm)
U_B (m/s)
Re_B=1000
t (ms)
(a) 0.48 mm
0.80/1.5
0.80/2.2
(b) 0.80 mm

Figure 3:

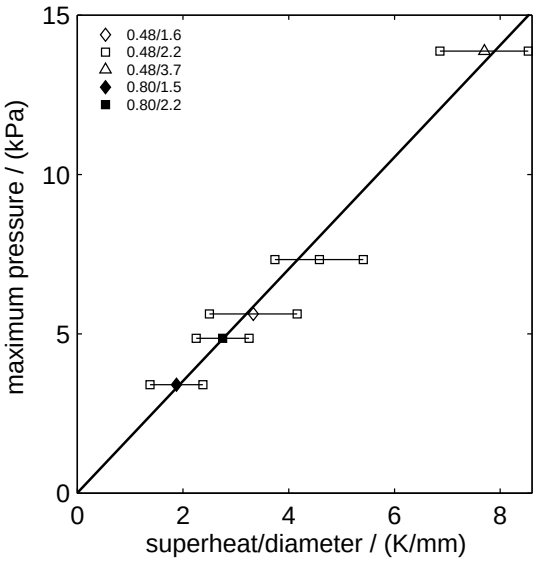
0.48/1.6
0.48/2.2
0.48/3.7
0.80/1.5
0.80/2.2
maximum pressure / (kPa)
superheat/diameter / (K/mm)
0
5
10
15
0
2
4
6
8

Figure 4:

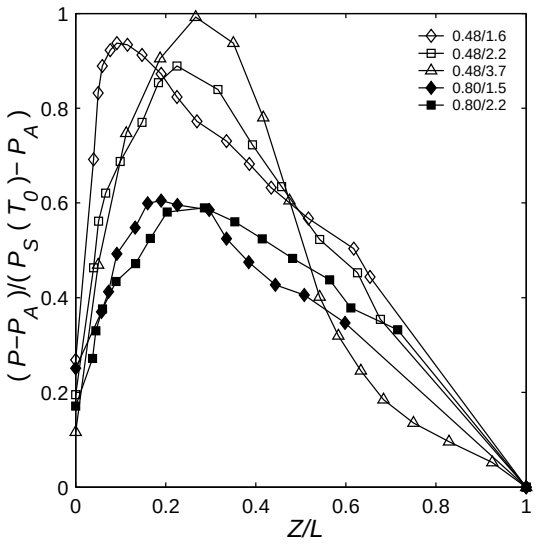

Figure 5:

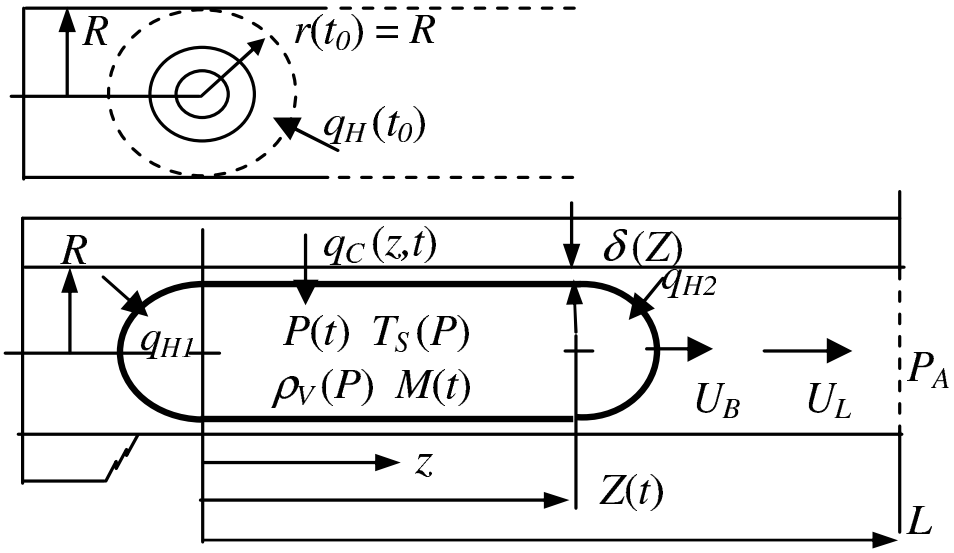

Figure 6:

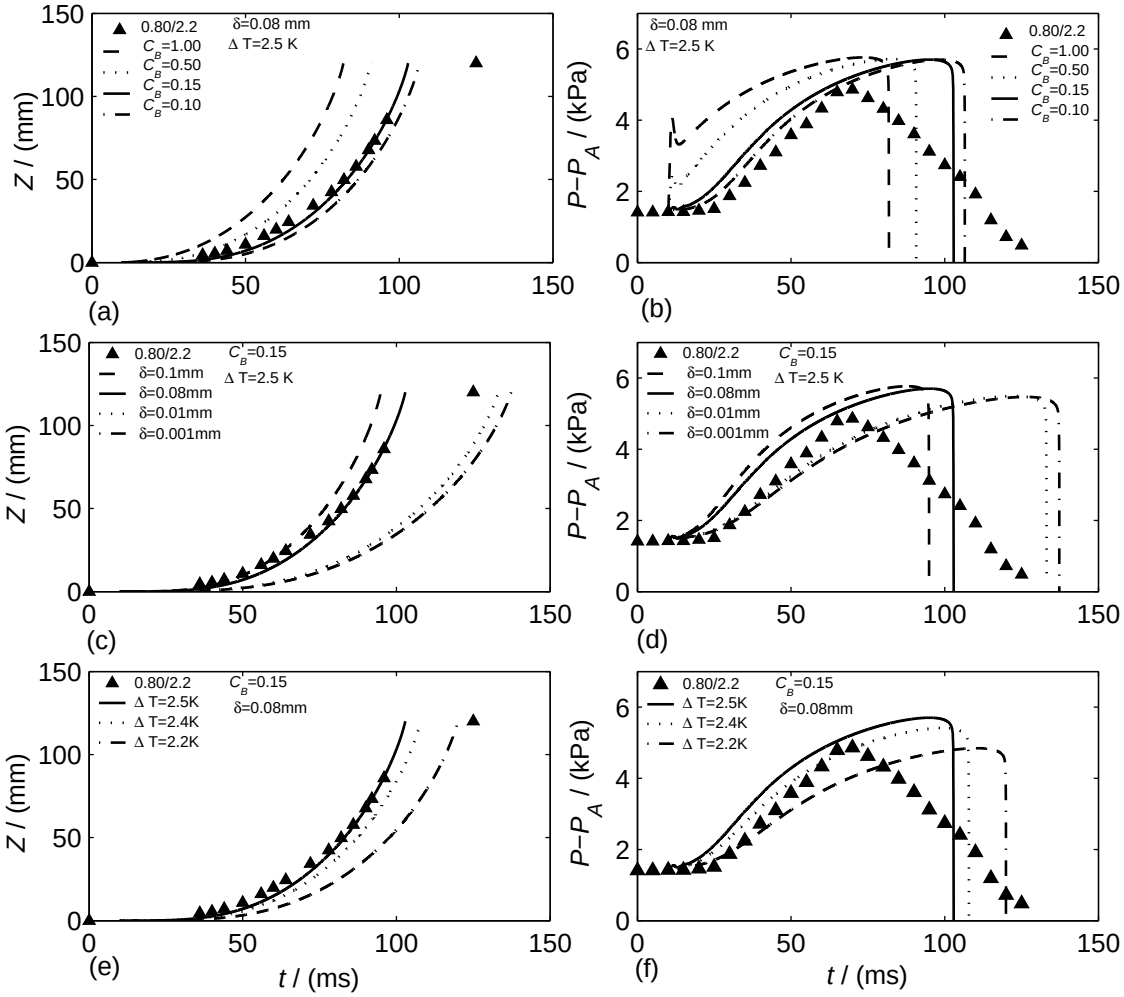
0.80/2.2
δ=0.08 mm
Δ T=2.5 K
C_B=1.00
C_B=0.50
C_B=0.15
C_B=0.10
Z / (mm)
P−P_A / (kPa)
(a)
(b)
δ=0.1mm
δ=0.08mm
δ=0.01mm
δ=0.001mm
(c)
(d)
Δ T=2.5K
Δ T=2.4K
Δ T=2.2K
(e)
(f)
t / (ms)

Figure 7:

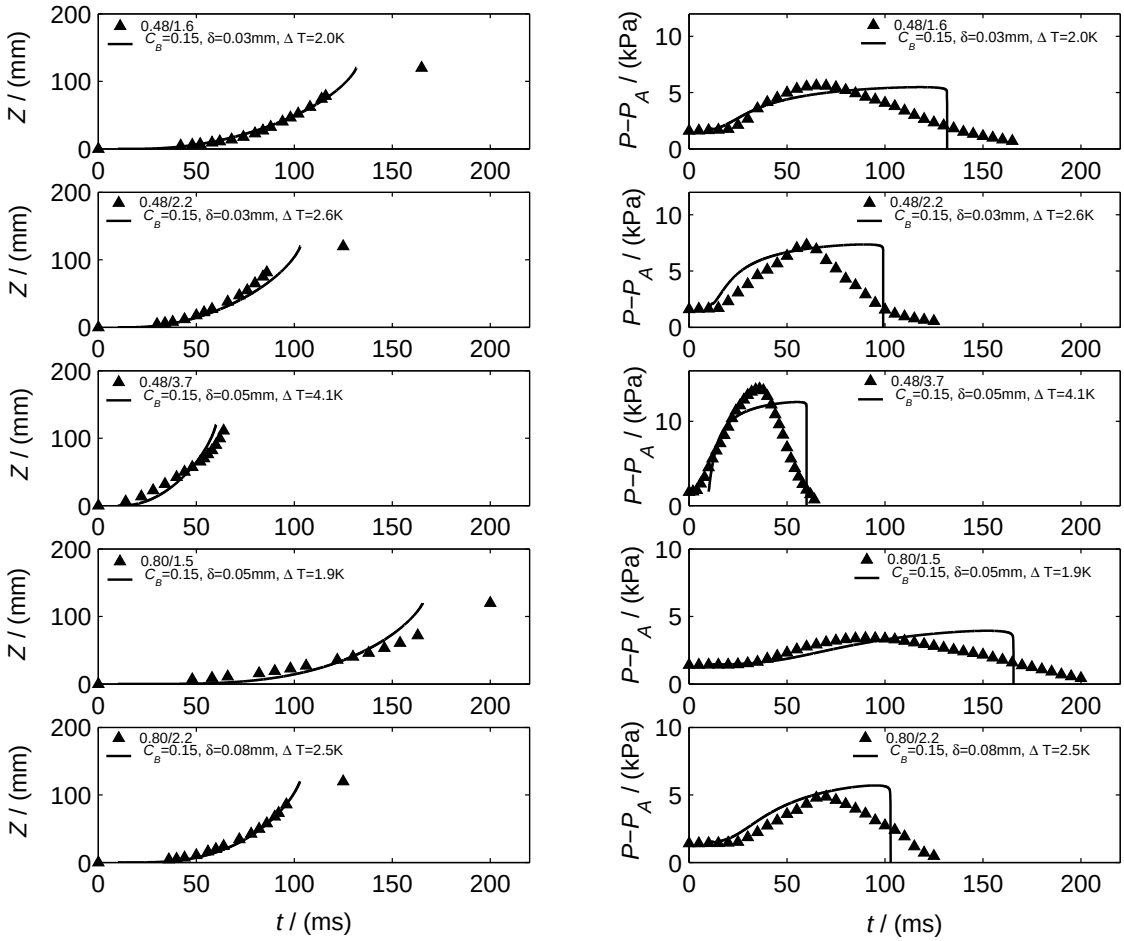
0.48/1.6
C_B=0.15, δ=0.03mm, Δ T=2.0K
0.48/2.2
C_B=0.15, δ=0.03mm, Δ T=2.6K
0.48/3.7
C_B=0.15, δ=0.05mm, Δ T=4.1K
0.80/1.5
C_B=0.15, δ=0.05mm, Δ T=1.9K
0.80/2.2
C_B=0.15, δ=0.08mm, Δ T=2.5K
Z / (mm)
P–P_A / (kPa)
t / (ms)

Figure 8:

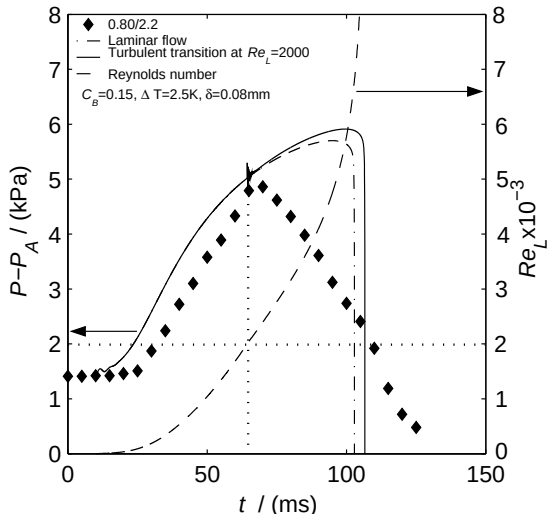
0.80/2.2
Laminar flow
Turbulent transition at Re_L=2000
Reynolds number
C_B=0.15, Δ T=2.5K, δ=0.08mm
$P-P_A$ / (kPa)
Re_L x10^{-3}
t / (ms)
0
50
100
150
1
2
3
4
5
6
7
8

Figure 9:

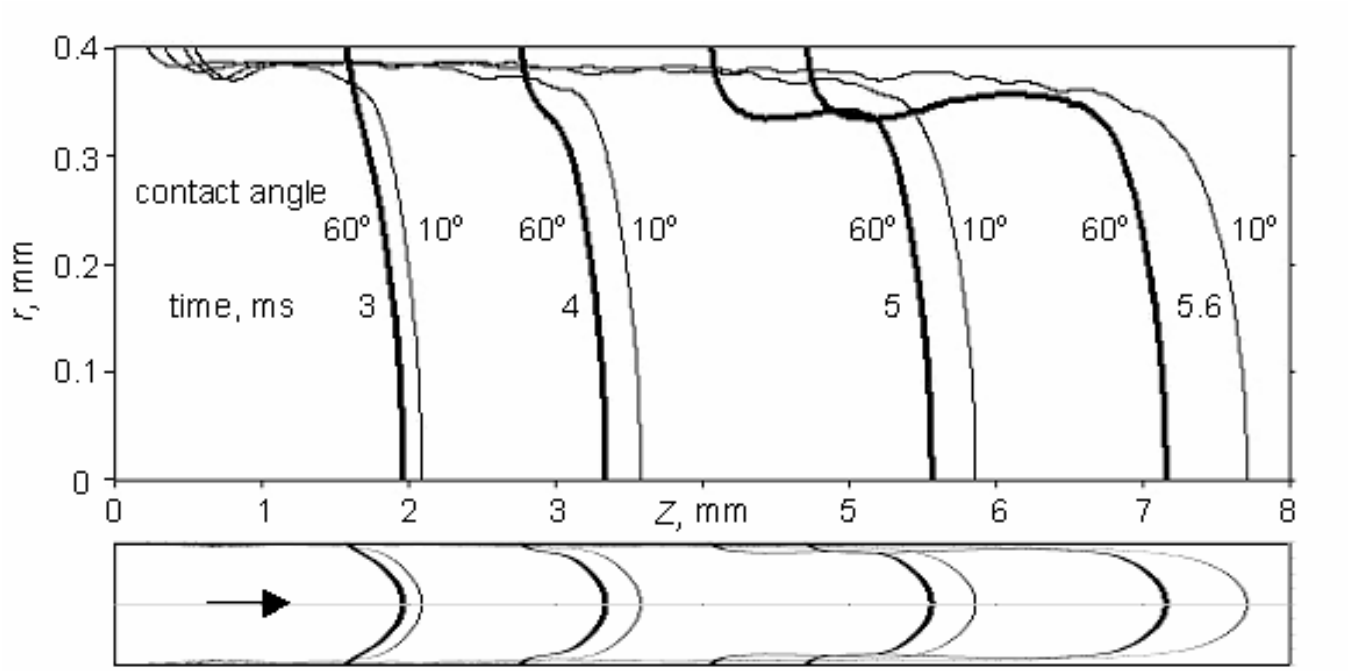
0.4
0.3
0.2
0.1
0
r, mm
contact angle
60°
10°
60°
10°
60°
10°
60°
10°
time, ms
3
4
5
5.6
0
1
2
3
Z, mm
5
6
7
8

Figure 10:

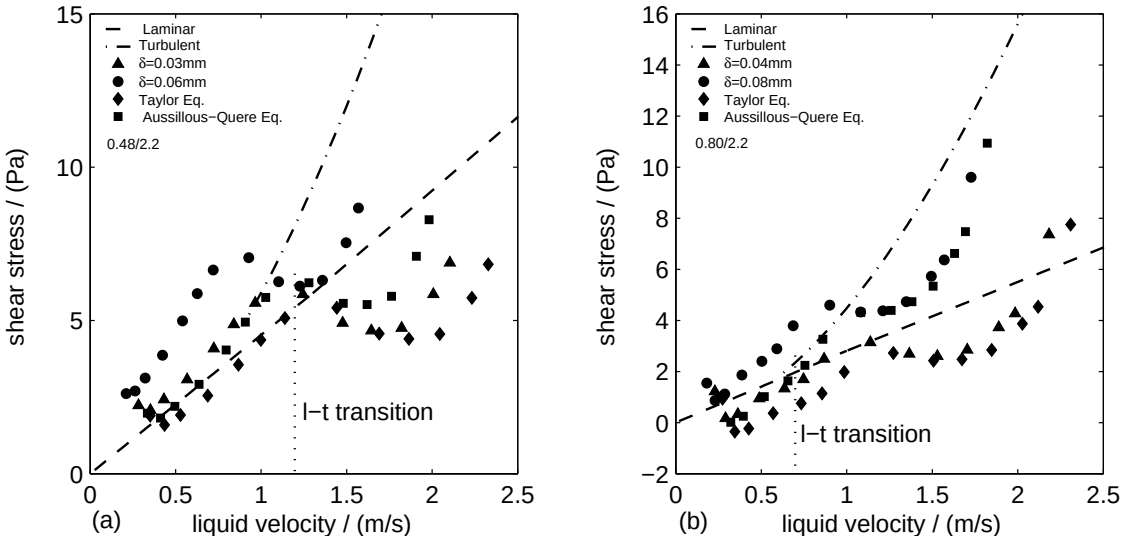
Laminar
Turbulent
δ=0.03mm
δ=0.06mm
Taylor Eq.
Aussillous−Quere Eq.
0.48/2.2
shear stress / (Pa)
l−t transition
(a)
liquid velocity / (m/s)
Laminar
Turbulent
δ=0.04mm
δ=0.08mm
Taylor Eq.
Aussillous−Quere Eq.
0.80/2.2
shear stress / (Pa)
l−t transition
(b)
liquid velocity / (m/s)

Figure 11:

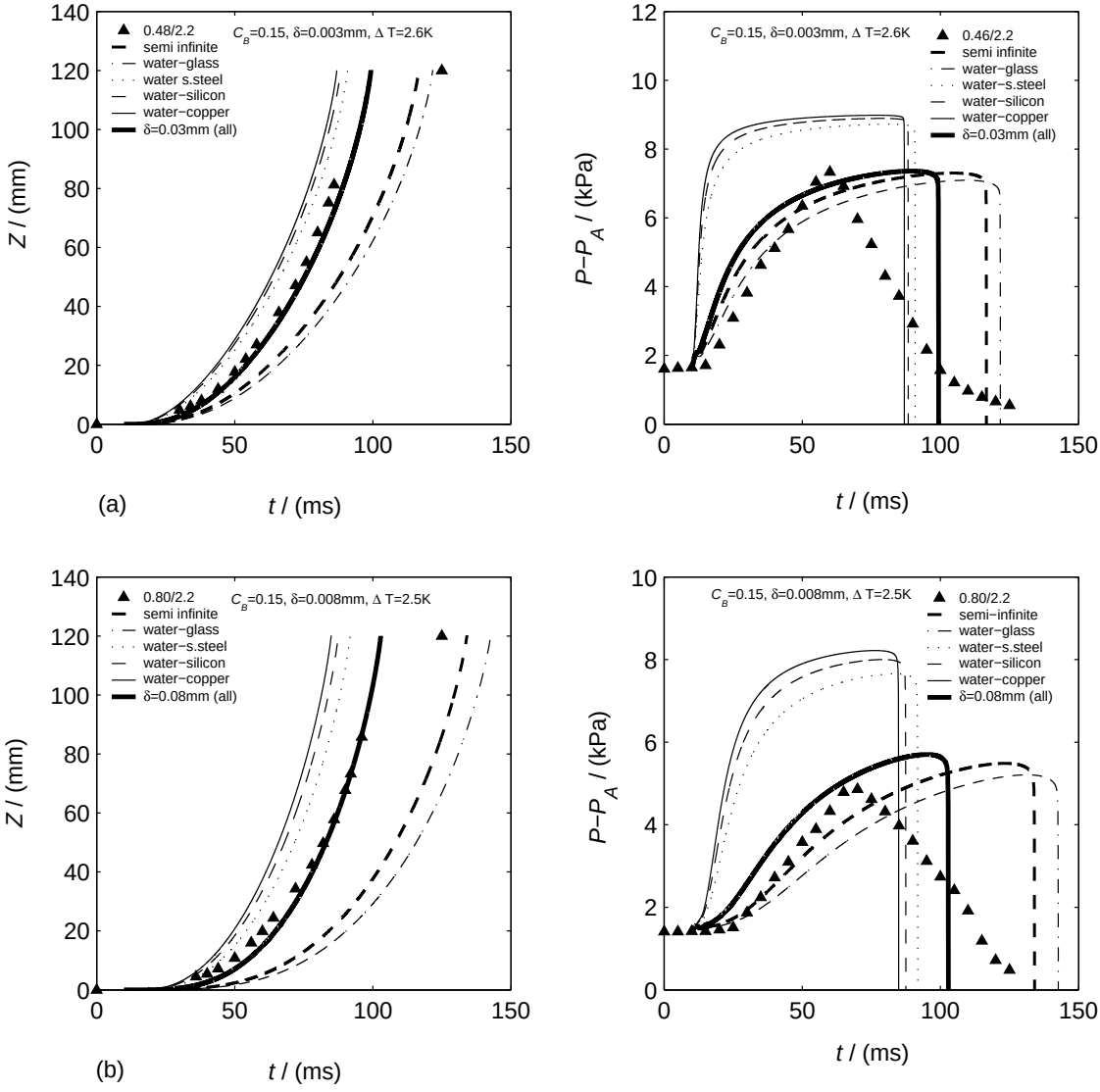
0.48/2.2
C_B=0.15, δ=0.003mm, Δ T=2.6K
semi infinite
water−glass
water s.steel
water−silicon
water−copper
δ=0.03mm (all)
Z / (mm)
(a)
t / (ms)
0.46/2.2
P−P_A / (kPa)
0.80/2.2
C_B=0.15, δ=0.008mm, Δ T=2.5K
water−s.steel
δ=0.08mm (all)
(b)

Figure 12:

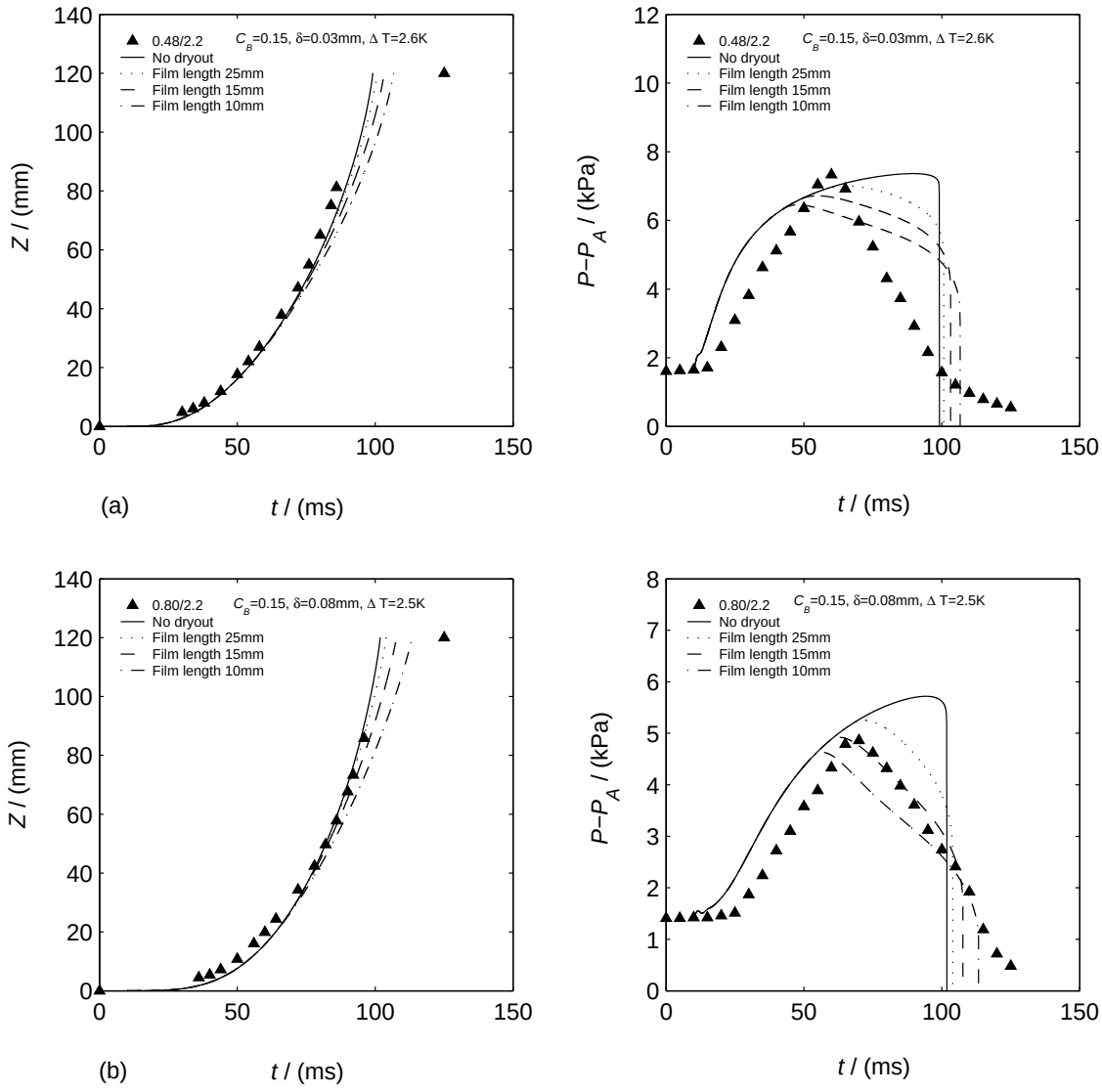
0.48/2.2 C_B=0.15, δ=0.03mm, Δ T=2.6K
No dryout
Film length 25mm
Film length 15mm
Film length 10mm
Z / (mm)
P–P_A / (kPa)
t / (ms)
(a)
0.80/2.2 C_B=0.15, δ=0.08mm, Δ T=2.5K
No dryout
Film length 25mm
Film length 15mm
Film length 10mm
Z / (mm)
P–P_A / (kPa)
t / (ms)
(b)

Figure 13:

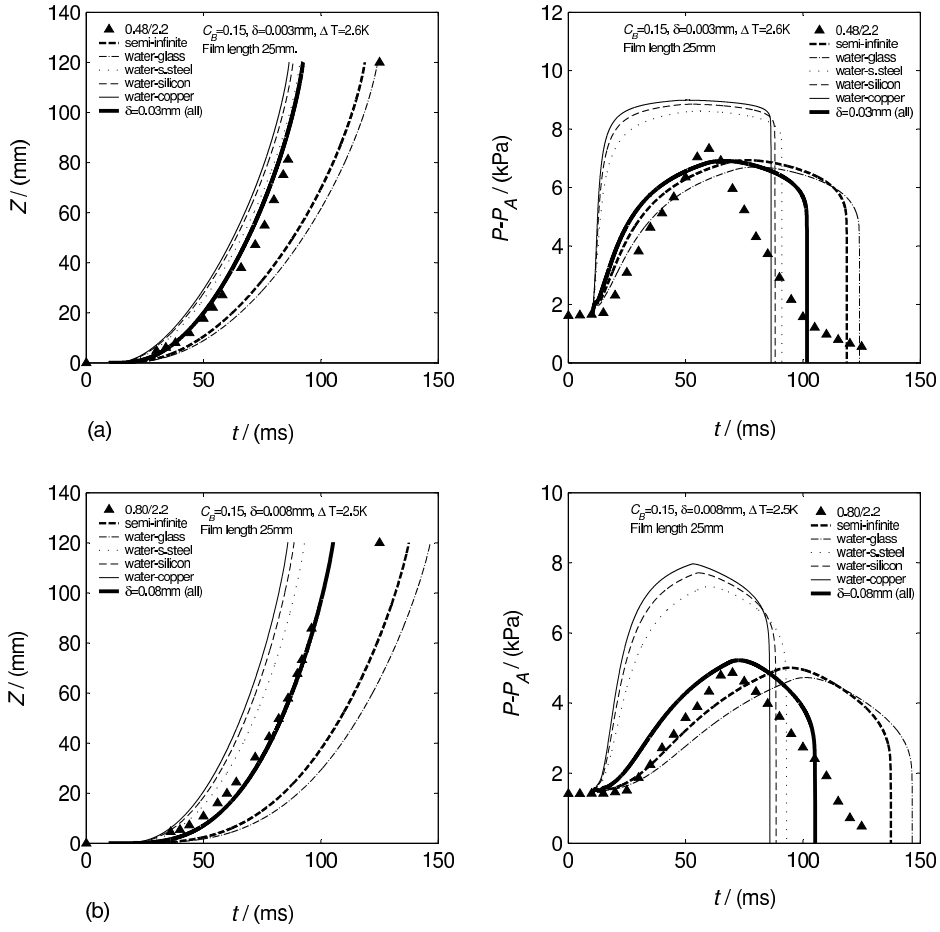
0.48/2.2
semi-infinite
water-glass
water-s.steel
water-silicon
water-copper
δ=0.03mm (all)
C_B=0.15, δ=0.003mm, ΔT=2.6K
Film length 25mm.
Z / (mm)
t / (ms)
(a)
$P-P_A$ / (kPa)
0.80/2.2
δ=0.08mm (all)
C_B=0.15, δ=0.008mm, ΔT=2.5K
(b)

Figure 14:

Parameter	Run				
	0.48/1.6	0.48/2.2	0.48/3.7	0.80/1.5	0.80/2.2
$\Delta T = T_0 - T_S(P_0)$, K	2.0	2.6	4.1	1.9	2.5
C_B	0.15	0.15	0.15	0.15	0.15
δ, mm optimised	0.030	0.030	0.050	0.050	0.080
δ, mm Eq.(21)	0.006	0.009	0.12	0.0008	0.016

Table 1:

t ms	U_B m/s	$\dot{U}_B$ m/s^2	Ca	Bo Eq.(25)	Bo_{MI} Eq.(26)	δ/R simulated $3R$	$4R$	δ/R Eq.(21)	δ/R Eq.(24) $C_M = 0.8$	δ/R Eq.(27)	δ/R Eq.(29) $C_{\delta_0} = 1$
3	1.20	500	5.8×10^{-3}	1.3	1.0	0.035	n/a	0.039	0.059	0.013	0.017
4	1.82	830	8.6×10^{-3}	2.2	1.2	0.053	0.039	0.050	0.069	0.014	0.014
5	2.95	2000	1.4×10^{-2}	5.2	1.5	0.070	0.060	0.066	0.077	0.015	0.012
5.5	5.00	12000	2.4×10^{-2}	31	2.4	0.092	0.077	0.087	0.080	0.116	0.009

Table 2: